



**HAL**  
open science

# Bulk Glassy GeTe<sub>2</sub>: A Missing Member of the Tetrahedral GeX<sub>2</sub> Family and a Precursor for the Next Generation of Phase-Change Materials

Andrey Tverjanovich, Maxim Khomenko, Chris Benmore, Maria Bokova, Anton Sokolov, Daniele Fontanari, Mohammad Kassem, Takeshi Usuki, Eugène Bychkov

► **To cite this version:**

Andrey Tverjanovich, Maxim Khomenko, Chris Benmore, Maria Bokova, Anton Sokolov, et al.. Bulk Glassy GeTe<sub>2</sub>: A Missing Member of the Tetrahedral GeX<sub>2</sub> Family and a Precursor for the Next Generation of Phase-Change Materials. *Chemistry of Materials*, 2021, 33 (3), pp.1031-1045. 10.1021/acs.chemmater.0c04409 . hal-04210136

**HAL Id: hal-04210136**

**<https://hal.science/hal-04210136>**

Submitted on 18 Oct 2023

**HAL** is a multi-disciplinary open access archive for the deposit and dissemination of scientific research documents, whether they are published or not. The documents may come from teaching and research institutions in France or abroad, or from public or private research centers.

L'archive ouverte pluridisciplinaire **HAL**, est destinée au dépôt et à la diffusion de documents scientifiques de niveau recherche, publiés ou non, émanant des établissements d'enseignement et de recherche français ou étrangers, des laboratoires publics ou privés.

# Bulk Glassy GeTe<sub>2</sub>: A Missing Member of the Tetrahedral GeX<sub>2</sub> Family and a Precursor for the Next Generation of Phase-Change Materials

Andrey Tverjanovich, Maxim Khomenko, Chris J. Benmore, Maria Bokova, Anton Sokolov, Daniele Fontanari, Mohammad Kassem, Takeshi Usuki, and Eugene Bychkov\*



Cite This: *Chem. Mater.* 2021, 33, 1031–1045



Read Online

ACCESS |



Metrics & More

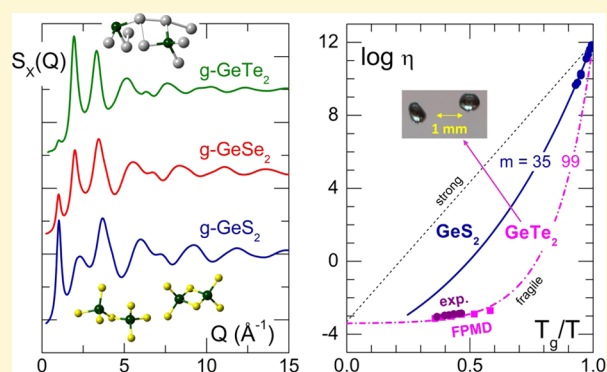


Article Recommendations



Supporting Information

**ABSTRACT:** Vitreous germanium disulfide GeS<sub>2</sub> and diselenide GeSe<sub>2</sub> belong to canonical chalcogenide glasses extensively studied over the past half century. Their high-temperature orthorhombic polymorphs are congruently melting compounds, and the tetrahedral crystal and glass structure is largely preserved in the melt. In contrast, the ditelluride counterpart is absent in the Ge–Te phase diagram, which shows only a single compound, monotelluride GeTe. Phase-change materials based on GeTe have become a technologically important class of solids, and their structure and properties are also widely studied. Surprisingly, very scarce information is available for alloys having GeTe<sub>2</sub> stoichiometry. Using a fast quenching procedure in silica capillaries, high-energy X-ray diffraction, and Raman spectroscopy supported by first-principles simulations, we show that bulk glassy GeTe<sub>2</sub> differs substantially from the lighter GeX<sub>2</sub> members, revealing 46% of trigonal germanium, 31% of three-fold coordinated tellurium, and only 20% of edge-sharing tetrahedra or pyramids. The fraction of homopolar Ge–Ge bonds is low; however, the population of dominant Te–Te dimers and Te<sub>n</sub> oligomers,  $n \leq 10$ , appears to be significant. The complex structural and chemical topology of g-GeTe<sub>2</sub> is directly related to the thermodynamic metastability of germanium ditelluride, schematically represented by the following reaction:  $\text{GeTe}_2 \rightleftharpoons \text{GeTe} + \text{Te}$ . Disproportionation is complete above liquidus in the temperature range of semiconductor–metal transition, and the dense metallic GeTe<sub>2</sub> liquid, mostly consisting of five-fold coordinated Ge species, exhibits high fluidity, strong fragility ( $m = 99 \pm 5$ ), and presumably a fast structural transformation rate combined with low atomic mobility in the vicinity of the glass transition temperature, favorable for reliable long-term data retention in nonvolatile memories. The observed and predicted characteristic features make GeTe<sub>2</sub> a promising precursor for the next generation of phase-change materials, especially coupled with additional metal doping, depolymerizing the tetrahedral interconnected glass network and accelerating (sub)nanosecond crystallization.



## INTRODUCTION

Vitreous germanium dichalcogenides, GeX<sub>2</sub>, X = S, Se, are canonical IV–VI glasses often considered as heavier counterparts of SiO<sub>2</sub> and GeO<sub>2</sub> tetrahedral glassy oxides. In contrast to the latter, the GeX<sub>4</sub> tetrahedra in a disordered network<sup>1–6</sup> share both corners, CS-GeX<sub>4</sub>, and edges, ES-GeX<sub>4</sub>, similar to those in high-temperature GeS<sub>2</sub> and GeSe<sub>2</sub> orthorhombic polymorphs,<sup>7,8</sup> while the low-temperature or high-pressure forms only have CS-entities.<sup>9,10</sup> These two germanium dichalcogenides are characterized by congruent melting,<sup>11,12</sup> and the GeX<sub>2</sub> melts also reveal a tetrahedral structure with four-fold Ge and a two-fold coordinated chalcogen local environment.<sup>1,13</sup> The Ge–Te phase diagram differs significantly from the Ge–S and Ge–Se binary systems.<sup>14,15</sup> The only stable compound appears to be monotelluride GeTe, extensively studied over the last 20 years as a crucial component of phase-change materials (PCMs) used for optical

storage, nonvolatile random-access memories, and neuromorphic computing.<sup>16–19</sup> Rhombohedral GeTe, space group  $R\bar{3}m$ ,<sup>20</sup> has a strong Peierls distortion of the rock salt cubic structure with three short, 2.827 Å, and three long, 3.167 Å, Ge–Te bonds and is often considered as a compound with effective trigonal coordination of both germanium and tellurium,<sup>21</sup> also called as a defective octahedral environment. Metastable GeTe<sub>2</sub> with cubic  $\beta$ -cristobalite lattice, space group  $Fd\bar{3}m$ , was found to occur in a narrow temperature range, 450

Received: November 16, 2020

Revised: January 5, 2021

Published: January 15, 2021



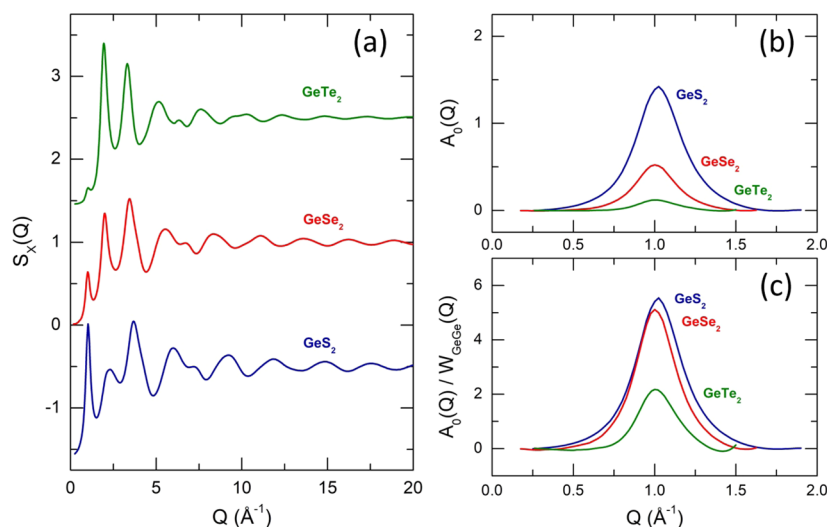


**Figure 1.** (a) Faber–Ziman X-ray structure factors  $S_X(Q)$  of glassy dichalcogenides:  $\text{GeS}_2$  (blue curve),  $\text{GeSe}_2$  (red curve), and  $\text{GeTe}_2$  (green curve); (b) isolated FSDPs derived using the subtraction procedure;<sup>3,53</sup> and (c) the FSDP amplitude  $A_0(Q)$  normalized by the  $Q$ -dependent Ge–Ge X-ray weighting factor,  $A_0(Q)/W_{\text{GeGe}}(Q)$ .

$\leq T < 520$  K, and only for crystallized thin films with a maximum thickness of  $\approx 6$   $\mu\text{m}$ .<sup>22,23</sup> For thicker films and at  $T \gtrsim 520$  K, a disproportionation reaction takes place:  $\text{GeTe}_2 \rightarrow \text{GeTe} + \text{Te}$ .

The glass-forming range in the  $\text{Ge}_x\text{Te}_{1-x}$  system is limited by  $0.1 \leq x \leq 0.25$ .<sup>24</sup> Amorphous thin films can be obtained by sputtering, thermal evaporation, or pulsed laser deposition up to  $x = 0.76$ .<sup>25,26</sup> Using a specially designed quenching procedure in thin-walled silica capillaries, we were able to obtain bulk  $\text{GeTe}_2$  glasses of a few mg total mass; Figure S1. This report represents their spectroscopic and structural characterization using Raman scattering and high-energy X-ray diffraction measurements supported by first-principles simulations. We compare the obtained results with sulfide and selenide glassy counterparts discussing the origin of the observed similarities and differences in the  $\text{GeX}_2$  glass family. Above liquidus,  $\text{GeTe}_2$  transforms into a dense metallic liquid dramatically different from tetrahedral  $\text{GeS}_2$  and  $\text{GeSe}_2$  melts. The first-principles molecular dynamics reproduces well the available diffraction data and reveals a structural evolution on semiconductor–metal transition. High fluidity and liquid fragility and specific short- and intermediate-range structures suggest fast structural transformations in the melt, making  $\text{GeTe}_2$  a promising precursor for the next generation of phase-change materials.

## EXPERIMENTAL SECTION

**Glassy  $\text{GeTe}_2$  Preparation.** A crystalline sample of  $\text{GeTe}_2$  composition was synthesized from high-purity elements Ge (99.999%, Neyco) and Te (99.999%, Cerac) in an evacuated silica tube at  $\approx 1220$  K in a rocking furnace. A small quantity of the synthesized alloy (2–3 mg) was placed in a silica capillary, which was evacuated and sealed. The capillary was heated to a temperature of 150 K above liquidus. Then, both the ends of the capillary were opened, and tiny melt droplets dropped down onto a metallic plate cooled with liquid nitrogen. The splat quenching procedure was performed in a dry argon atmosphere.

**Diffraction Measurements.** High-energy X-ray diffraction measurements were carried out using a 6-ID-D beamline at the Advanced Photon Source (Argonne National Laboratory). The X-ray energy was 100.233 keV, and the wavelength was 0.123696 Å. A two-dimensional (2D) setup was used for data collection with a Varex area

detector,  $2880 \times 2880$  pixels, and pixel size of  $150 \mu\text{m} \times 150 \mu\text{m}$ . The expose time was  $0.1 \text{ s} \times 3000$  frames, using one dark field image file followed by five light files (dark field subtracted). The sample image was saturated with a full beam; attenuation was set to 0.2 for diffraction measurements. The two-dimensional diffraction patterns were reduced using the Fit2D software.<sup>27</sup> The measured background intensity was subtracted, and corrections were made for the different detector geometries and efficiencies, sample self-attenuation, and Compton scattering using standard procedures,<sup>28</sup> providing the X-ray structure factor  $S_X(Q)$ .

**Raman Spectroscopy Measurements.** Raman spectra of bulk glassy  $\text{GeTe}_2$  were measured in backscattering geometry using a Senterra Raman spectrometer (Bruker) equipped with a microscope. The spectra were excited by a 785 nm laser with power 1 mW and recorded in the  $75$ – $1500 \text{ cm}^{-1}$  spectral range (reliable data are above  $100 \text{ cm}^{-1}$ ). The spectrometer resolution was  $3 \text{ cm}^{-1}$ . Bulk glass references  $\text{Ge}_x\text{Te}_{1-x}$ ,  $0.1 \leq x \leq 0.25$ , were measured using a LabRam HR microRaman spectrometer (Jobin Yvon Horiba Group). Raman scattering was excited by a 785 nm solid-state laser and recorded in the  $50$ – $850 \text{ cm}^{-1}$  spectral range. The laser power was  $30 \mu\text{W}$ , and the acquisition time was  $2 \text{ s} \times 300$  frames. Two to three spectra were registered for each sample at different positions to verify the sample homogeneity and the absence of photoinduced phenomena.

**First-Principles Simulations.** The Born–Oppenheimer molecular dynamics implemented within the CP2K package<sup>29</sup> was used for structural modeling of the diffraction data. The generalized gradient approximation and the PBE0 hybrid<sup>30,31</sup> exchange–correlation functional combining the exact Hartree–Fock and density functional theory (DFT) solutions were used. The Grimme dispersion corrections D3BJ<sup>32</sup> were also applied, having a positive effect for glassy and liquid tellurides.<sup>33,34</sup> The applied first-principles molecular dynamics (FPMD) technique was similar to that reported previously.<sup>35,36</sup> The initial atomic configurations for glassy  $\text{GeTe}_2$  were created and optimized using the RMC\_POT++ code<sup>37</sup> against the derived X-ray structure factor  $S_X(Q)$  to obtain good agreement with the experimental data. The size of the cubic simulation box at room temperature, containing 450 atoms (150 Ge and 300 Te), was chosen to match the experimental number density. Further optimization was carried out using density functional theory (DFT), applying the molecularly optimized correlation consistent polarized triple-zeta valence TZVP basis set along with the norm-conserving relativistic Goedecker–Teter–Hutter-type pseudopotentials.<sup>38</sup> FPMD simulations were started at 300 K. To deal with a canonical NVT ensemble, a Nosé–Hoover<sup>39,40</sup> chain was employed as a thermostat. The PBE0 systems were heated up to 1000 K using 100 K steps for

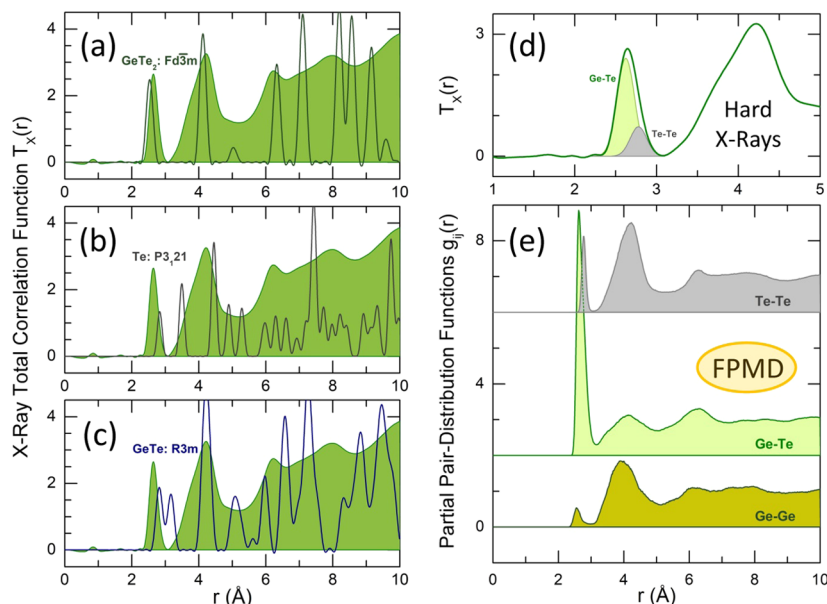


**Figure 2.** Correlation functions in  $r$ -space. The X-ray total correlation function  $T_X(r)$  for glassy  $\text{GeTe}_2$  (highlighted in green) plotted together with crystalline references: (a) metastable cubic  $\text{GeTe}_2$ , space group  $Fd\bar{3}m$ ;<sup>22</sup> (b) trigonal  $\text{Te}$ ,  $P3_121$ ;<sup>59</sup> (c) rhombohedral  $\text{GeTe}$ ,  $R\bar{3}m$ ;<sup>20</sup> (d) a two-peak Gaussian fit of the nearest-neighbor correlations in  $g\text{-GeTe}_2$ , the Ge–Te NNs highlighted in light green, and the Te–Te NNs in light gray; (e) FPMD partial pair-distribution functions  $g_{ij}(r)$  for glassy  $\text{GeTe}_2$ : Te–Te (light gray), Ge–Te (light green), and Ge–Ge (dark yellow).

10–15 ps each. At 500 and 1000 K, the systems were equilibrated for 25–35 ps and cooled to 300 K using the same temperature steps and the simulation time. Final equilibration and data collection at 300 K was done for 30–45 ps. Diffusion/viscosity simulations were carried out in the 800–1300 K temperature range for at least 40–50 ps at each temperature. The connectivity and ring statistics were analyzed using the R.I.N.G.S.<sup>41</sup> and modified connectivity<sup>42</sup> codes. The pyMolDyn<sup>43</sup> program applying the Dirichlet–Voronoi tessellation was used for the calculation of microscopic voids and cavities.

The DFT calculations of vibrational spectra were carried out using Gaussian 16 software.<sup>44</sup> The structural optimization and harmonic vibrational frequency calculations were performed for size-limited clusters,  $\text{Ge}_2\text{Te}_7\text{H}_6$ ,  $\text{Ge}_2\text{Te}_8\text{H}_6$ ,  $\text{Ge}_2\text{Te}_6\text{H}_4$ ,  $\text{Ge}_2\text{Te}_6\text{H}_6$ ,  $\text{GeTe}_8\text{H}_4$ ,  $\text{GeTe}_{12}\text{H}_4$ ,  $\text{GeTe}_5\text{H}_4$ ,  $\text{Ge}_2\text{Te}_4\text{H}_2$ ,  $\text{GeTe}_6\text{H}_3$ , and  $\text{GeTe}_9\text{H}_3$ , some of them in different conformations. The Becke three-parameter hybrid exchange functional<sup>45</sup> and the Lee–Yang–Parr correlation functional (B3LYP)<sup>46</sup> were applied for these simulations. The small-core relativistic pseudopotential basis set (cc-pVTZ-PP)<sup>47</sup> and the effective core potentials<sup>48</sup> were employed for cluster geometry optimization and Raman intensity calculations. Most of the structures were optimized using the tight convergence option ensuring adequate convergence and reliability of computed wavenumbers. Extra quadratically convergent self-consistent field procedure<sup>49</sup> was used for difficult convergence cases. Further details of the DFT simulations are published elsewhere.<sup>50–52</sup>

## RESULTS AND DISCUSSION

**High-Energy X-ray Diffraction.** X-ray structure factor  $S_X(Q)$  of bulk  $g\text{-GeTe}_2$  is shown in Figure 1 in comparison with those of its lighter counterparts,<sup>3,53</sup>  $g\text{-GeS}_2$  and  $g\text{-GeSe}_2$

$$S_X(Q) = w_{\text{GeGe}}(Q)S_{\text{GeGe}}(Q) + w_{\text{GeTe}}(Q)S_{\text{GeTe}}(Q) + w_{\text{TeTe}}(Q)S_{\text{TeTe}}(Q) \quad (1)$$

where  $w_{ij}(Q)$  is  $Q$ -dependent X-ray weighting coefficients and  $S_{ij}(Q)$  is the Faber–Ziman partial structure factors. All structure factors exhibit a striking similarity above  $\approx 3 \text{ \AA}^{-1}$  and characteristic changes below, including a systematic shift of the  $S_X(Q)$  oscillations to lower  $Q$  with increasing chalcogen

atomic number  $n_X$  and size  $r_X$ . The first sharp diffraction peak, FSDP, at  $Q_0 \approx 1.0 \text{ \AA}^{-1}$  systematically decreases in amplitude with  $n_X$ , but its position  $Q_0$  remains essentially intact. On the contrary, the amplitude of the principle peak, PP, increases with  $n_X$ , and the PP position shifts from  $Q_1 \approx 2.29 \text{ \AA}^{-1}$  ( $g\text{-GeS}_2$ ) to  $1.95 \text{ \AA}^{-1}$  ( $g\text{-GeTe}_2$ ). We also note pronounced damping of the high- $Q$  oscillations with increasing  $n_X$ . The observed  $S_X(Q)$  for bulk  $g\text{-GeTe}_2$  is similar to that for a thermally co-evaporated  $\text{Ge}_{0.33}\text{Te}_{0.67}$  thin film.<sup>26</sup>

The FSDP evolution is shown in Figure 1b, derived using the background subtraction described previously.<sup>3,53</sup> In the cases of  $g\text{-GeS}_2$  and  $g\text{-GeSe}_2$ , the main contribution to the FSDP comes from Ge–Ge correlations, verified both experimentally and theoretically.<sup>2,5,6,54</sup> Consequently, the FSDP amplitude  $A_0(Q)$  normalized by the  $Q$ -dependent Faber–Ziman X-ray weighting factor for Ge–Ge atomic pairs,  $A_0(Q)/w_{\text{GeGe}}(Q)$ , appears to be pretty similar for the two glasses; Figure 1c. A 12-fold difference in  $A_0(Q)$  between  $g\text{-GeS}_2$  and  $g\text{-GeTe}_2$  decreased by a factor of 4 using the above normalization; nevertheless, the ratio  $A_0(Q)/w_{\text{GeGe}}(Q)$  [ $g\text{-GeS}_2$ ]/ $A_0(Q)/w_{\text{GeGe}}(Q)$  [ $g\text{-GeTe}_2$ ] =  $2.9 \pm 0.4$  indicates several contributions to the FSDP of glassy germanium ditelluride.

The PP amplitude is often related to the packing efficiency<sup>55</sup> and enhanced extended-range order<sup>56</sup> and systematically increases in high-pressure experiments.<sup>57,58</sup> On the contrary, the macroscopic number density for  $g\text{-GeX}_2$  decreases with the atomic number  $n_X$ ,  $0.03605 \text{ atoms \AA}^{-3}$  ( $\text{GeS}_2$ )  $\rightarrow$   $0.03314 \text{ atoms \AA}^{-3}$  ( $\text{GeSe}_2$ )  $\rightarrow$   $0.02937 \text{ atoms \AA}^{-3}$  ( $\text{GeTe}_2$ ), certainly dominated by the increasing chalcogen size  $r_X$ . In addition, the main contribution to the PP comes from the X–X partial structure factors  $S_{XX}(Q)$ , as shown by a systematic shift of the PP position  $Q_1$  toward lower  $Q$  with  $n_X$  and  $r_X$ . The average Faber–Ziman X-ray weighting coefficients,  $\langle W_{XX}(Q) \rangle$ , substantially increase with  $n_X$  by a factor of  $\approx 3$ , from  $0.192 \pm 0.006$  ( $\text{GeS}_2$ ) to  $0.621 \pm 0.003$  ( $\text{GeTe}_2$ ), explaining the observed trend.

**Table 1.** Nearest-Neighbor Interatomic Distances  $r_{ij}$  and Partial Coordination Numbers  $N_{ij}$  in Experimental and FPMD Data for Glassy  $\text{GeTe}_2$ 

Ge–Ge		Ge–Te		Te–Te		$N_{\text{Ge-X}}$	$N_{\text{Te-X}}$
$r_{ij}$ (Å)	$N_{ij}$	$r_{ij}$ (Å)	$N_{ij}$	$r_{ij}$ (Å)	$N_{ij}$		
Experimental X-ray Data							
$a$	$a$	2.62(1)	3.46(10)	2.78(2)	0.50(10)	3.46(10)	2.23(14)
FPMD Data							
2.51	0.13(3)	2.60	3.40(10)	2.74	0.61(3)	3.53(11)	2.31(11)

<sup>a</sup>The Ge–Ge contribution is too weak to be quantified reliably.

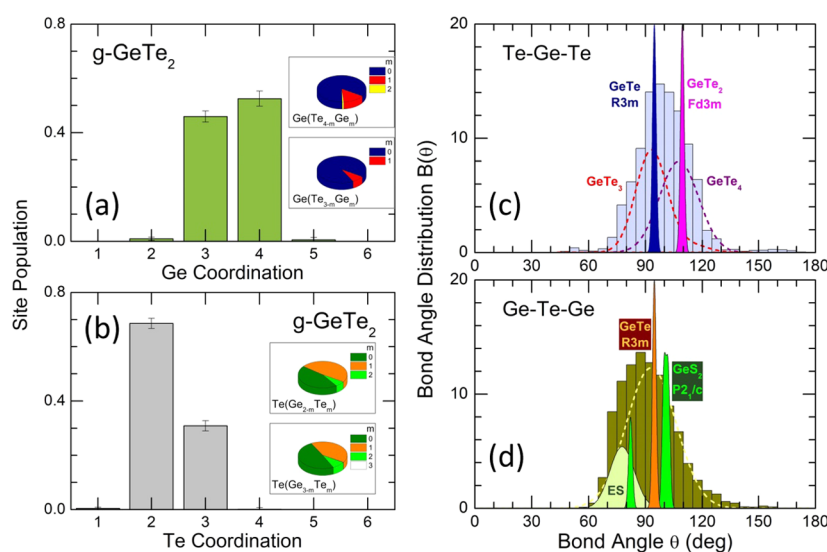


**Figure 3.** Coordination and angular dependences in glassy  $\text{GeTe}_2$ . Coordination distributions at (a) Ge and (b) Te sites; the insets show the NN distributions for tetrahedral and trigonal central Ge atom and two- and three-fold coordinated central Te. Bond angle distributions  $B(\theta)$  for (c) Te–Ge–Te and (d) Ge–Te–Ge triplets plotted together with those for crystalline references: metastable cubic  $\text{GeTe}_2$ , sg  $Fd\bar{3}m$ ;<sup>22</sup> rhombohedral  $\text{GeTe}$ , sg  $R\bar{3}m$ ;<sup>20</sup> and orthorhombic  $\text{HT-GeS}_2$ , sg  $P21/c$ .<sup>7</sup> See the text for further details.

The X-ray total correlation function  $T_X(r)$  obtained through the usual Fourier transform is shown in Figure 2a–c

$$T_X(r) = 4\pi\rho_0 r + \frac{2}{\pi} \int_0^{Q_{\max}} Q[S_X(Q) - 1] \sin QrM(Q)dQ \quad (2)$$

where  $M(Q)$  is a modification function,  $\rho_0$  is the experimental number density, and  $Q_{\max} = 25 \text{ \AA}^{-1}$ . The derived  $T_X(r)$  is plotted together with crystalline references: metastable cubic  $\text{GeTe}_2$ , space group (sg)  $Fd\bar{3}m$ ;<sup>22</sup> trigonal Te, sg  $P3_121$ ;<sup>59</sup> and rhombohedral  $\text{GeTe}$ , sg  $R\bar{3}m$ .<sup>20</sup> The asymmetric peak at 2.64 Å, well separated from more distant correlations, mostly corresponds to Ge–Te nearest neighbors (NNs). The peak position is located between the Ge–Te interatomic distances in metastable cubic  $\text{GeTe}_2$  (2.54 Å)<sup>22,23</sup> and short Ge–Te NN separations in rhombohedral  $\text{GeTe}$  (2.83 Å).<sup>20</sup> A broad asymmetric second neighbor peak is centered at 4.22 Å. The Te–Te (c- $\text{GeTe}_2$ ) or Te–Te/Ge–Ge (c- $\text{GeTe}$ ) atomic pairs in crystalline tellurides exhibit similar distances. Nevertheless, a long low- $r$  tail is missing in crystalline binaries. A distinct peak at 6.2 Å also has a certain similarity with Ge–Te second neighbor correlations (6.3 Å) in metastable  $\text{GeTe}_2$ . Rhombohedral  $\text{GeTe}$  is characterized by Te–Te/Ge–Ge and Ge–Te third-neighbor correlations at 5.97 and 6.57 Å, respectively.

A two-peak Gaussian fitting of the NN feature at 2.64 Å reproduces well its asymmetric shape; Figure 2d. The main contribution at 2.62 Å is clearly related to short Ge–Te atomic pairs with the partial coordination number  $N_{\text{Ge-Te}}^S = 3.46 \pm$

0.10. The origin of the second contribution at 2.78 Å is less certain. It could be long Ge–Te NN correlations,  $N_{\text{Ge-Te}}^L = 0.93 \pm 0.10$ , but the total germanium coordination in this case appears to be above four. The Te–Te NN contacts are also possible both structurally (the Te–Te distances in trigonal tellurium are similar, 2.835 Å;<sup>59</sup> Figure 2b) and chemically, following a dissociation reaction  $\text{GeTe}_2 \rightleftharpoons \text{GeTe} + \text{Te}$ . The Te–Te partial coordination number seems to be realistic,  $N_{\text{Te-Te}} = 0.50 \pm 0.10$ . Besides, a mixture of the two scenarios cannot be excluded, as well as asymmetric NN distributions in contrast to symmetric Gaussians. The first-principles molecular dynamics and Raman spectroscopy supported by DFT calculations yield decisive evidence in favor of a partial disproportionation.

**First-Principles Molecular Dynamics.** Experimental and derived FPMD interference functions  $Q[S_X(Q) - 1]$  are shown in Figure S2a. We note a good agreement between the two data sets. The PP amplitude of the FPMD structure factor is slightly underestimated, which is a common feature of small boxes used in first-principles modeling caused by heavy simulation costs. The partial structure factors  $S_{ij}(Q)$ , Figure S2b, confirm that contributions to the FSDP are from Ge–Ge and Ge–Te partials, and the amplitude of the principle peak is essentially related to the  $S_{\text{TeTe}}(Q)$  and  $S_{\text{GeGe}}(Q)$  functions.

The partial pair-distribution functions  $g_{ij}(r)$  are shown in Figure 2e. The NN feature at 2.65 Å is composed of Ge–Ge (2.51 Å,  $N_{\text{Ge-Ge}} = 0.13 \pm 0.03$ ), Ge–Te (2.60 Å,  $N_{\text{Ge-Te}} = 3.40 \pm 0.10$ ), and Te–Te (2.74 Å,  $N_{\text{Te-Te}} = 0.61 \pm 0.03$ ) NN

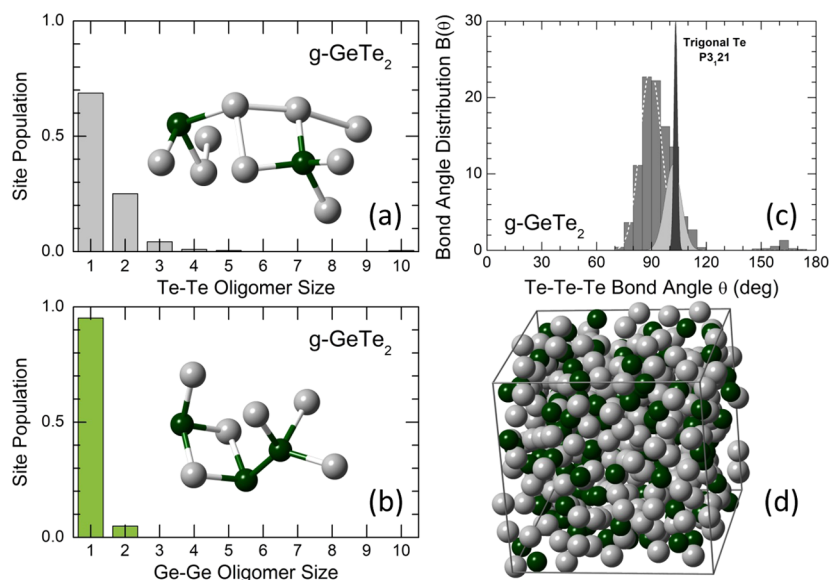


**Figure 4.** Connectivity analysis of glassy  $\text{GeTe}_2$ . Size distribution in (a)  $\text{Te}_n$  and (b)  $\text{Ge}_n$  oligomers; (c) intrachain  $\text{Te}-\text{Te}-\text{Te}$  angles for  $\text{Te}_n$  oligomeric chains,  $n \geq 3$ ; and (d) snapshot of the 450 atom FPMD simulation box at 300 K. The intrachain angle in trigonal tellurium<sup>59</sup> is also shown in (c). The insets in (a) and (b) reveal typical oligomer motifs in glassy  $\text{GeTe}_2$ .

contributions, consistent with the experimental results; Table 1. Weak Ge–Ge atomic pairs are hardly visible in experimental  $T_X(r)$  overlapping with intense Ge–Te nearest neighbors. The total germanium coordination appears to be below 4,  $N_{\text{Ge-X}} = N_{\text{Ge-Te}} + N_{\text{Ge-Ge}} = 3.53$ , indicating that populations of four-fold and trigonal Ge species are comparable; Figure 3a. The local environment of germanium is mixed (see the inset in Figure 3a); however, pure telluride ( $m = 0$ ) polyhedra  $\text{Ge}(\text{Te}_{4-m}\text{Ge}_m)$  and  $\text{Ge}(\text{Te}_{3-m}\text{Ge}_m)$  are dominant, 85 and 92%, respectively. The majority of tellurium, 69%, has two-fold coordination, and the fractions of Ge–Te–Ge and Ge–Te–Te connections are nearly identical; Figure 3b. A similar situation also exists for three-fold coordinated tellurium; the probability of a Te-rich environment around the central Te atom,  $\text{Te}(\text{Ge}_{3-m}\text{Te}_m)$  and  $m \geq 2$ , is less than  $\approx 9\%$ . The Ge-centered polyhedra are mostly corner-sharing; the fraction of the ES-units is rather small,  $20 \pm 5\%$  vs  $\approx 50\%$  in g- $\text{GeSe}_2$  and g- $\text{GeTe}_2$ .<sup>7,8</sup>

The Te–Ge–Te and Ge–Te–Ge angular distributions  $B(\theta)$ s are shown in Figure 3c,d together with  $B(\theta)$ s of crystalline references: cubic  $\text{GeTe}_2$ , rhombohedral  $\text{GeTe}$ , and orthorhombic HT- $\text{GeSe}_2$ . The  $B_{\text{TeGeTe}}(\theta)$  in glassy  $\text{GeTe}_2$  is rather symmetric and centered at  $98^\circ$ . However, the apparent symmetry hides two nearly equally populated distributions related to  $\text{GeTe}_3$  trigonal units and  $\text{GeTe}_4$  tetrahedra, the red and purple dashed lines, respectively, in Figure 3c. The  $B_{\text{TeGeTe}}(\theta)$  maxima for trigonal and tetrahedral germanium are similar to crystalline references: rhombohedral  $\text{GeTe}$ ,  $94^\circ$ , and metastable cubic  $\text{GeTe}_2$ ,  $109^\circ$ .<sup>20,22,23</sup> We should however note that  $B_{\text{TeGeTe}}(\theta)$  for rhombohedral  $\text{GeTe}$  was derived only for short Ge–Te interatomic distances (2.83 Å) without taking into account long Ge–Te correlations (3.17 Å).

The tetrahedral orientational order parameter  $q$ <sup>60,61</sup> allows for additional information on the local geometry of four-fold coordinated  $\text{GeTe}_4$  species to be obtained

$$q = 1 - \frac{3}{8} \sum_{j=1}^3 \sum_{k=j+1}^4 \left( \cos \psi_{jk} + \frac{1}{3} \right)^2 \quad (3)$$

where  $\psi_{jk}$  is the angle formed by the lines joining the central germanium atom of a given  $\text{GeTe}_4$  unit and its nearest Te neighbors  $j$  and  $k$ . The average value of  $q$  changes between 0 for an ideal gas and  $q = 1$  for a perfect tetrahedral network. The  $P(q)$  probability distribution function is shown in Figure S3. The regular or distorted tetrahedra having  $q \geq 0.87$  appear to be a clear majority, 90.3%. The remaining  $\text{GeTe}_4$  polyhedra,  $0.45 \leq q \leq 0.76$ , have a defect octahedral local geometry with two missing Te neighbors around the central germanium atom and two types of the Te–Ge–Te angles,  $146^\circ \leq \theta_{\text{Oh}}(1) \leq 170^\circ$  and  $53^\circ \leq \theta_{\text{Oh}}(2) \leq 102^\circ$ ; the inset in Figure S3. An ideal defect octahedron  $\text{GeTe}_4$ ,  $\theta_{\text{Oh}}(1) = \pi$  and  $\theta_{\text{Oh}}(2) = \pi/2$ , has  $q = 5/8$ , that is, just in the middle of the nontetrahedral  $q$ -range. The minority nontetrahedral  $\text{GeTe}_4$  species are hardly visible on the respective  $B_{\text{TeGeTe}}(\theta)$  angular dependences; Figure 3c.

The  $B_{\text{TeGeTe}}(\theta)$  bond angle distribution associated with polyhedral connectivity exhibits an asymmetric shape with the main contribution at  $94^\circ$ , which is very similar to the trigonal connectivity of  $\text{GeTe}_3$  pyramids in rhombohedral  $\text{GeTe}$  (the peak highlighted in orange in Figure 3d). The tetrahedral connections in metastable  $\text{GeTe}_2$  with the bond angle  $\theta(\text{GeTeGe}) = \pi$  are not consistent with the derived FPMD angular function. A low-angle  $B_{\text{TeGeTe}}(\theta)$  contribution, highlighted in light green, is related to edge-sharing Ge–Te units, mostly ES- $\text{Ge}(\text{Te}_{4-m}\text{Ge}_m)$ . The observed value  $\theta(\text{GeTeGe}) = 78^\circ$  is similar to that for the ES-tetrahedra ( $82^\circ$ ) in high-temperature  $\text{GeS}_2$  polymorph consisting of ES- and CS-units;<sup>7</sup> the corresponding peaks are highlighted in bright green in Figure 3d. The orthorhombic  $\text{GeSe}_2$  analog shows an even closer ES-value,  $80^\circ$ ,<sup>8</sup> associated with the increasing chalcogen size  $r_X$ . Consequently, the tetrahedral connectivity in g- $\text{GeTe}_2$  is reminiscent of lighter  $\text{GeX}_2$  polymorphs than that of metastable cubic  $\text{GeTe}_2$ . We also note a large fraction of both Te–Ge–Te and Ge–Te–Ge bond angles  $\theta \cong 90^\circ$ , especially for  $\text{GeTe}_3$  units; Figure 4a,b.

The connectivity analysis shows that 94% of Ge and Te atoms form a continuous disordered network. A small population of homopolar Ge–Ge bonds occurs as Ge–Ge

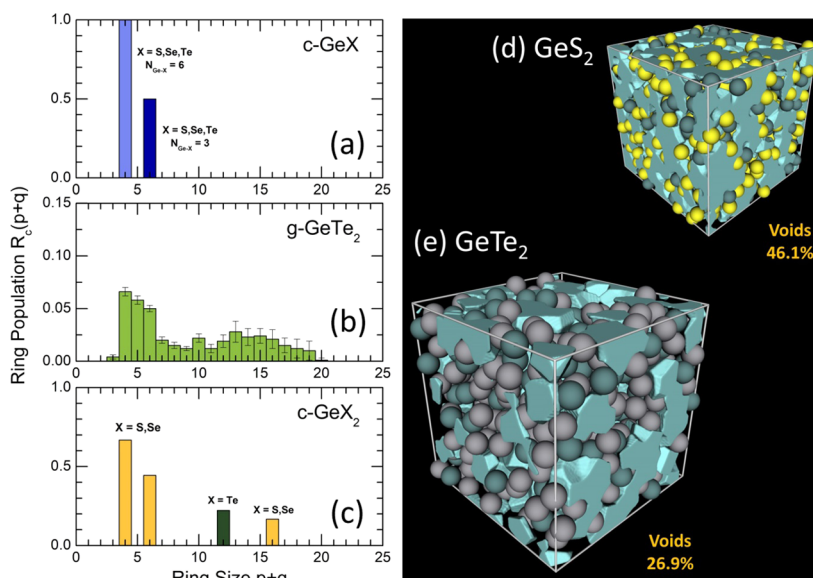


**Figure 5.** Rings and cavities in glassy  $\text{GeTe}_2$ . The ring population  $R_c(p+q)$ <sup>41</sup> in (a) orthorhombic<sup>62</sup> or rhombohedral<sup>20</sup>  $\text{GeX}$  ( $X = \text{S}, \text{Se}, \text{Te}$ ); (b) glassy  $\text{GeTe}_2$ ; and (c) orthorhombic  $\text{GeS}_2$ ,  $\text{GeSe}_2$ , and metastable cubic  $\text{GeTe}_2$ ;<sup>22</sup> the cavity distributions in (d)  $g\text{-GeS}_2$  and (e)  $g\text{-GeTe}_2$ , calculated using the *pyMolDyn* code.<sup>43</sup>

dimers; **Figure 4b**. A larger fraction of  $\text{Te}\text{--}\text{Te}$  bonds is seen through a variety of  $\text{Te}_n$  oligomers, where  $2 \leq n \leq 10$ , but the  $\text{Te}\text{--}\text{Te}$  dimers have the highest population; **Figure 4a**. A few oligomeric  $\text{Te}_n$  chains,  $n \geq 3$ , have different conformations evidenced by the asymmetric  $B_{\text{TeTeTe}}(\theta)$  bond angle distribution; **Figure 4c**. Just one quarter of them shows the intrachain bond angle comparable with that in trigonal tellurium,  $\theta(\text{TeTeTe}) = 103.2^\circ$ ;<sup>59</sup> the remaining three quarters have the  $\text{Te}\text{--}\text{Te}\text{--}\text{Te}$  angle peaked at  $\approx 90^\circ$ , **Figure 4a,c**.

The spatial distribution of trigonal  $\text{Ge}_{3\text{F}}$  and tetrahedral  $\text{Ge}_{4\text{F}}$  species is not completely random. A non-negligible part,  $\approx 40\%$  ( $\text{Ge}_{3\text{F}}$ ) and  $\approx 30\%$  ( $\text{Ge}_{4\text{F}}$ ), forms connected fragments  $\text{Ge}_{3\text{F}}\text{--}\text{Te}$  (the maximum size of 16 atoms) and  $\text{Ge}_{4\text{F}}\text{--}\text{Te}$  (up to 30 atoms). The remaining population is separated by  $4.7 \leq r_{\text{Ge}\text{--}\text{Ge}} \leq 6.9 \text{ \AA}$  for the average random  $\text{Ge}_{3\text{F}(4\text{F})}\text{--}\text{Ge}_{3\text{F}(4\text{F})}$  distance of  $6.4 \text{ \AA}$ .

The intermediate-range order in glassy  $\text{GeTe}_2$  is given by the statistics of  $\text{Ge}_p\text{Te}_q$  rings; **Figure 5b**. The derived ring population  $R_c(p+q)$ <sup>41</sup> differs significantly from the expected four-fold rings in rhombohedral  $\text{GeTe}$ ,<sup>20,62</sup> when short and long  $\text{Ge}\text{--}\text{Te}$  distances are taking into account, or six-fold entities, if only short  $\text{Ge}\text{--}\text{Te}$  separations are considered, **Figure 5a**, and 12-membered  $\text{Ge}_6\text{Te}_6$  units in metastable cubic  $\text{GeTe}_2$ . Except for the topological disorder, the  $R_c(p+q)$  population is reminiscent of ring statistics in orthorhombic  $\text{GeS}_2$  or  $\text{GeSe}_2$  polymorphs,<sup>7,8</sup> **Figure 5c**, with the highest fraction of “square” rings, remembering the abundant bond angles  $\theta(\text{TeGeTe}) \approx \theta(\text{GeTeGe}) \approx \pi/2$ , substantially populated six-fold entities, and broad distribution of big rings centered at  $p+q = 14 \pm 2$ . Similar  $R_c(p+q)$  populations were found for lighter tetrahedral glassy counterparts  $\text{GeX}_2$ <sup>6,41</sup> but with an enhanced population of big rings,  $20 \lesssim p+q \lesssim 30$ .

The cavity distribution is shown in **Figure 5d,e**. The total volume of microscopic voids and cavities,  $V_c$ , normalized to the volume of the FPMD simulation box, appears to be 26.9%, that is, significantly lower than that in  $g\text{-GeS}_2$  (46.1%). Consequently, the packing density in glassy  $\text{GeTe}_2$  appears to be higher than that in glassy  $\text{GeS}_2$  and probably  $\text{GeSe}_2$ , coherent with the increasing amplitude of the principle peak in  $S_X(Q)$

with the chalcogen size  $r_X$  and atomic number  $n_X$ ; **Figure 1a**. We should also note that a similar  $V_c$  was found for liquid and glassy  $\text{Ge}_{0.15}\text{Te}_{0.85}$  while amorphous and liquid  $\text{GeTe}$  has a much smaller cavity volume,  $6.4 \leq V_c \leq 11.3\%$ .<sup>63</sup>

The derived FPMD results using hybrid PBE0 exchange–correlation functional for bulk glassy  $\text{GeTe}_2$  differ substantially from those of the reverse Monte-Carlo (RMC) modeling of an amorphous  $\text{Ge}_{0.33}\text{Te}_{0.67}$  thin film.<sup>26</sup> In the latter case, the total coordination number of Ge was constrained to be 4. As a result, the total tellurium coordination was found to be  $N_{\text{Te}\text{--}\text{X}}^{\text{RMC}} = N_{\text{Te}\text{--}\text{Ge}}^{\text{RMC}} + N_{\text{Te}\text{--}\text{Te}}^{\text{RMC}} = 1.07(25) + 0.99(15) = 2.06 \pm 0.29$ , and the partial  $\text{Ge}\text{--}\text{Ge}$  coordination number,  $N_{\text{Ge}\text{--}\text{Ge}}^{\text{RMC}} = 1.9 \pm 0.4$ , appears to be by a factor of  $\approx 15$  higher than the FPMD value,  $N_{\text{Ge}\text{--}\text{Ge}}^{\text{FPMD}} = 0.13 \pm 0.03$ ; **Table 1**. On the contrary, the RMC modeling of  $\text{Ga}_{0.143}\text{Ge}_{0.143}\text{Te}_{0.714}$  glass with a similar tellurium content exhibits no  $\text{Ge}\text{--}\text{Ge}$  and  $\text{Ga}\text{--}\text{Ga}$  homopolar bonds and higher tellurium coordination,  $N_{\text{Te}\text{--}\text{X}} = 2.35 \pm 0.10$ .<sup>64</sup> The reported FPMD results for amorphous and liquid  $\text{Ge}\text{--}\text{Te}$  alloys depend on the choice of the exchange–correlation functional. The use of standard PBE or PBEsol functionals without van der Waals corrections overestimates the interatomic distances and the total tellurium coordination,  $N_{\text{Te}\text{--}\text{X}} = 3.1\text{--}3.8$ , for  $\text{Te}$ -rich alloys.<sup>34,63</sup> The Grimme dispersion corrections<sup>65</sup> improve the two types of parameters,<sup>33,34</sup> but a better agreement with experiments yields hybrid functionals,<sup>34,66</sup> in particular, BLYP.<sup>67,68</sup> The applied PBE0 hybrid functional provides similar simulation results as BLYP. Nevertheless, independent verification of the FPMD modeling needs alternative structural methods such as vibrational spectroscopy.

**Raman Spectroscopy.** The Raman scattering supported by the DFT simulations of vibrational spectra was used to verify two main results of synchrotron diffraction and first-principles molecular dynamics: (a) the presence of  $\text{Te}\text{--}\text{Te}$  homopolar bonds and (b) the partial tetrahedral local coordination of germanium.

A typical Raman spectrum of bulk glassy  $\text{GeTe}_2$  between 100 and  $300 \text{ cm}^{-1}$  is shown in **Figure 6a**. Three characteristic features at 130, 160, and  $245 \text{ cm}^{-1}$  are similar to those

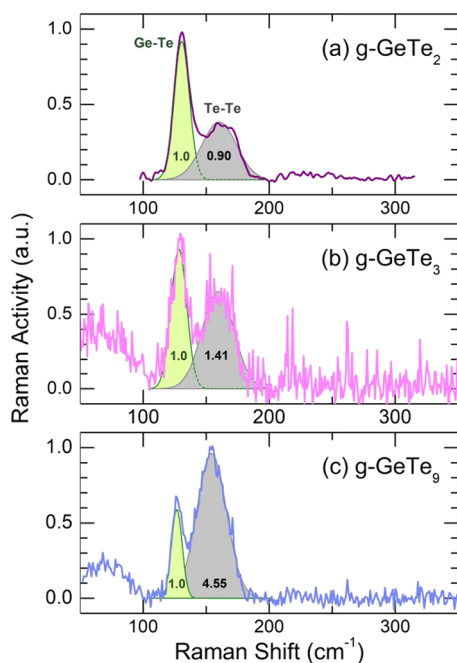


**Figure 6.** Experimental Raman spectra of bulk  $\text{Ge}_x\text{Te}_{1-x}$  glasses: (a)  $\text{GeTe}_2$  ( $x = 0.33$ ), (b)  $\text{GeTe}_3$  ( $x = 0.25$ ), and (c)  $\text{GeTe}_9$  ( $x = 0.10$ ). The  $130\text{ cm}^{-1}$  peak (light green) corresponds to  $A_1$  in-phase Ge–Te breathing in corner-sharing  $\text{CS-GeTe}_4$  tetrahedra; the  $160\text{ cm}^{-1}$  multimodal feature (light gray) contains multiple Te–Te stretchings in  $\text{Te}_n$  oligomers,  $2 \leq n \leq 8$ , and Ge–Te symmetric stretching in ES-tetrahedra and CS- and ES- $\text{GeTe}_3$  units. The bending vibrations are shown below  $100\text{ cm}^{-1}$  for glassy  $\text{GeTe}_3$  and  $\text{GeTe}_9$  measured using a Raman spectrometer with the low-frequency limit of  $50\text{ cm}^{-1}$ . The relative areas of the  $130$  and  $160\text{ cm}^{-1}$  peaks are also shown.

observed previously for  $\text{GeTe}_2$  thin films obtained by thermal evaporation, radiofrequency/magnetron sputtering, or pulsed laser deposition.<sup>25,69–71</sup> Compared to bulk  $\text{Ge}_x\text{Te}_{1-x}$  glasses,  $x \leq 0.25$ , the amplitudes of a relatively narrow  $130\text{ cm}^{-1}$  peak and a broader  $160\text{ cm}^{-1}$  line are reversed, Figure 6b,c,

confirming their assignment to Ge–Te and Te–Te stretching, respectively.<sup>25,69,72</sup> A broad poorly resolved feature at  $245\text{ cm}^{-1}$  of low intensity suggests multiple vibrational contributions.

The DFT modeling of a corner-sharing  $\text{CS-Ge}_2\text{Te}_7\text{H}_6$  dimer reveals that the  $130\text{ cm}^{-1}$  peak is related to  $A_1$  symmetric in-phase breathing of  $\text{CS-GeTe}_4$  tetrahedra, and the high-frequency asymmetric Ge–Te stretching vibrations are located in the range of  $200 \leq \omega \leq 250\text{ cm}^{-1}$ ; Figure 7a. Similar to glassy  $\text{GeS}_2$ , the  $A_1$  symmetric in-phase breathing in edge-sharing entities  $\text{ES-Ge}_2\text{Te}_6\text{H}_4$  is shifted to higher  $\omega = 142\text{ cm}^{-1}$ ; the asymmetric Ge–Te stretching frequencies are also spread over the  $190\text{--}250\text{ cm}^{-1}$  range; Figure 7b. The  $\text{GeTe}_8\text{H}_4$  and  $\text{GeTe}_{12}\text{H}_4$  clusters representing isolated Ge species cross-linking the Te chains exhibit strong Te–Te stretching modes in the vicinity of  $170 \pm 6\text{ cm}^{-1}$ , and the  $A_1$  symmetric Ge–Te stretching slightly shifted to lower wave-numbers ( $126 \pm 2\text{ cm}^{-1}$ ); Figure 7c. The trigonal  $\text{Ge}_{3F}\text{-Te}$  clusters are characterized by a blue shift of the  $A_1$  symmetric in-phase Ge–Te breathing in CS- and ES- $\text{GeTe}_3$  trigonal pyramids compared to CS- and ES-tetrahedra,  $\Delta\omega = +16 \pm 3\text{ cm}^{-1}$ ; Figure 7d–f. On the contrary, the Te–Te stretching frequencies in  $\text{Ge}_{3F}\text{-Te}$  entities exhibit a red shift,  $\Delta\omega = -6 \pm 3\text{ cm}^{-1}$ . Presumably, the weak Ge–Ge stretching in glassy  $\text{GeTe}_2$  is hardly visible. Typical Ge–Ge stretching frequencies are located between  $\omega_{\text{GeGe}} = 259\text{ cm}^{-1}$  in ethanelike  $\text{ETH-Ge}_2\text{S}_6$  units with homopolar Ge–Ge bonds<sup>73,74</sup> and  $\omega_{\text{GeGe}} = 275\text{ cm}^{-1}$  in amorphous Ge and  $\text{Ge}_{0.76}\text{Te}_{0.24}$  thin films.<sup>75</sup> The optimized DFT cluster  $\text{ETH-Ge}_2\text{Te}_6\text{H}_6$ , Figure S4, shows  $\omega_{\text{GeGe}} = 262\text{ cm}^{-1}$ , overlapping with asymmetric Ge–Te vibrations. The optimized geometry of Ge–Te size-limited clusters was found to be in good agreement with diffraction results and FPMD simulations; Table S1. The DFT results for  $\text{CS-GeTe}_6\text{H}_3$  and  $\text{CS-GeTe}_8\text{H}_4$  clusters are similar to those reported previously.<sup>72</sup>

Summarizing, we conclude that Raman spectroscopy supported by DFT modeling yields clear evidence in favor of tetrahedral Ge species reflected by the  $A_1$  symmetric in-phase

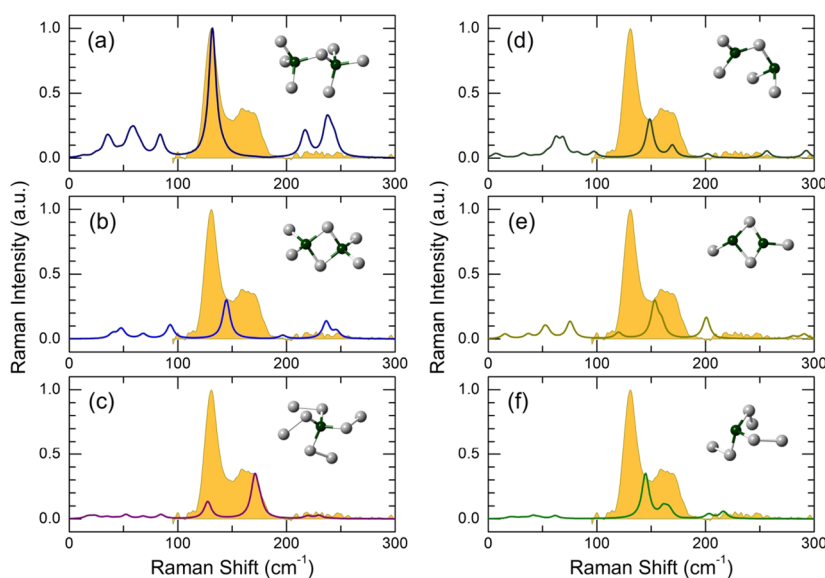


**Figure 7.** Experimental Raman spectra of glassy  $\text{GeTe}_2$ , highlighted in yellow in all panels and scaled DFT Raman spectra of selected optimized clusters: (a)  $\text{CS-Ge}_2\text{Te}_7$ , (b)  $\text{ES-Ge}_2\text{Te}_6$ , (c)  $\text{GeTe}_8$ , (d)  $\text{CS-Ge}_2\text{Te}_5$ , (e)  $\text{ES-Ge}_2\text{Te}_4$ , and (f)  $\text{GeTe}_6$ . The terminal hydrogen species are not shown, and H-related features are removed from the spectra.

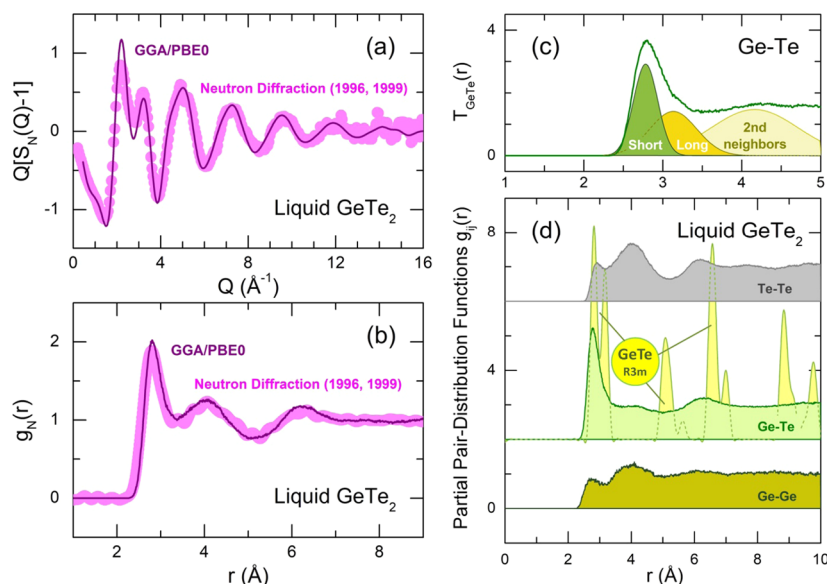


**Figure 8.** Experimental neutron data<sup>13,82</sup> and derived FPMD results for liquid GeTe<sub>2</sub> at 1000 K: (a) the interference function  $Q[S_N(Q) - 1]$ , (b) the pair-distribution function  $g_N(r)$ , (c) fitting the  $T_{\text{GeTe}}(r)$  partial, and (d) the FPMD partial pair-distribution functions  $g_{ij}(r)$ . The  $g_{\text{GeTe}}(r)$  partial function for rhombohedral GeTe, *sg R3m*,<sup>20</sup> is also shown in (d). See the text for further details.

Ge–Te breathing in CS-GeTe<sub>4</sub> at 131 cm<sup>-1</sup>. The A<sub>1</sub> symmetric in-phase Ge–Te breathing in ES-GeTe<sub>4</sub>, CS-, and ES-GeTe<sub>3</sub> units and multiple Te–Te stretching modes in Te<sub>*n*</sub> oligomers, 2 ≤ *n* ≤ 10, are responsible for the broad 160 cm<sup>-1</sup> peak. A dominant role of Te–Te vibrations in this feature shows the composition dependence of the 160 cm<sup>-1</sup> mode, remarkably increasing with the Te content; Figure 6.

A nearly equimolar mixture of tetrahedral GeTe<sub>4</sub> and trigonal GeTe<sub>3</sub> units coexisting with Te–Te dimers and oligomers, observed in glassy germanium ditelluride, appears to be a consequence of the disproportionation reaction  $\text{GeTe}_2 \rightleftharpoons \text{GeTe} + \text{Te}$  at high temperatures, observed previously for GeTe<sub>2</sub> thin films.<sup>22,23</sup> Amorphous germanium monotelluride mostly consists of three types of Ge polyhedra involving four-fold coordinated nontetrahedral Ge<sup>H</sup> and tetrahedral Ge<sup>T</sup> species and trigonal Ge<sup>III</sup> units.<sup>76,77</sup> In contrast to glassy GeTe<sub>2</sub>, the fraction of GeX<sub>4</sub> (X = Te, Ge) tetrahedra,  $f_T$ , is below  $f_T \lesssim 0.3$  and accompanied by formation of Ge–Ge homopolar bonds.<sup>63,77</sup> The three-fold coordinated GeTe<sub>3</sub> pyramidal units with the bond angles of  $\approx \pi/2$  are the remnants of the GeTe rhombohedral structure<sup>20</sup> when three short Ge–Te bonds (2.83 Å) become even shorter (2.62 Å, Table 1) and three long Ge–Te distances (3.17 Å) are pushed away into the second neighbor correlations. A similar trend was found in binary Ge<sub>*x*</sub>S<sub>1-*x*</sub> vitreous alloys<sup>3</sup> at  $x \rightarrow 0.5$ .

**Liquid GeTe<sub>2</sub> and a Semiconductor–Metal Transition.** Heating GeTe<sub>2</sub> above the liquidus temperature produces an anomalous increase in density and a semiconductor–metal transition,<sup>23,78</sup> similar to that in other Ge–Te compositions.<sup>79–81</sup> This liquid–liquid transition was not studied for GeTe<sub>2</sub>; however, the diffraction data just above liquidus are available,<sup>13,82,83</sup> and a density change was reported.<sup>84</sup> Both the neutron and X-ray structure factors are drastically different for liquid GeTe<sub>2</sub> compared to the bulk glass. The FPMD with hybrid GGA/PBE0 functional appears to be equally efficient for a metallic liquid and a semiconducting glass. Figure 8 shows the experimental neutron diffraction data<sup>13,82</sup> in both the *Q*- and *r*-space in comparison with the derived FPMD interference function  $Q[S_N(Q) - 1]$  and pair-distribution function  $g_N(r)$ ,

revealing a good agreement. In contrast to glassy GeTe<sub>2</sub>, the simulation yields a slightly overestimated principle peak PP at 2.16 Å<sup>-1</sup>. The amplitude of other oscillations and their periodicity are well reproduced.

A different shape of the structure factor with an intense PP and a weak second peak at 3.19 Å<sup>-1</sup>, markedly larger NN interatomic distances at 2.79 Å vs 2.64 Å in g-GeTe<sub>2</sub>, and broad correlations at 4.08 Å (4.22 Å in the bulk glass), filling the gap between the nearest and next-nearest neighbors, suggest a deep structural transformation between glassy and liquid GeTe<sub>2</sub>. This trend was not observed in the sulfide GeS<sub>2</sub> and selenide GeSe<sub>2</sub> counterparts, conserving their tetrahedral structure in the glass and liquid states.<sup>1–3,13</sup>

The partial pair-distribution functions for L-GeTe<sub>2</sub> are shown in Figure 8d. As expected, the first and second neighbor peaks become broader and overlap with each other. In particular, the  $g_{\text{GeTe}}(r)$  partial function exhibits an asymmetric shape with a long-*r* tail without a clear minimum. Fitting the  $T_{\text{GeTe}}(r)$  partial function, Figure 8c, yields two equally populated sites with short (2.78 Å) and long (3.13 Å) Ge–Te nearest-neighbor distances, which are very similar to those in rhombohedral GeTe,<sup>20</sup> except for the width and partial coordination numbers; the latter is smaller in liquid,  $N_{\text{Ge-Te}}^{\text{short}} \cong N_{\text{Ge-Te}}^{\text{long}} = 2.10 \pm 0.10$ ; see also the middle panel of Figure 8d. The second and third Ge–Te neighbor contributions in L-GeTe<sub>2</sub> are hardly resolved. Nevertheless, their positions and partial coordination numbers allow for important information on metallic GeTe<sub>2</sub> liquid to be extracted.

The second neighbor Ge–Te separations in rhombohedral GeTe are markedly longer (the main peak at 5.07 Å and the weak peak at 5.63 Å,  $N_{\text{Ge-Te}}^{2\text{nd,R}} = 8$ ) compared with those in liquid GeTe<sub>2</sub> at 4.16 Å,  $N_{\text{Ge-Te}}^{2\text{nd,L}} = 5.62$ ; Figure 8d. At the same time, the ratio  $N_{\text{Ge-Te}}^{2\text{nd,L}}/N_{\text{Ge-Te}}^{2\text{nd,R}} = 5.62/8.00 \cong N_{\text{Ge-Te}}^{\text{NN,L}}/N_{\text{Ge-Te}}^{\text{NN,R}} = 4.20/6.00 = 0.70$  appears to be similar in the two cases. In contrast, the difference in the third neighbor Ge–Te positions between liquid GeTe<sub>2</sub> and rhombohedral GeTe is rather small, 6.47 Å (L-GeTe<sub>2</sub>) vs 6.57 Å (the main peak in the crystal), comparable with a dense metallic liquid and a less-dense semiconducting crystal. These findings suggest a strong

**Table 2.** Nearest-Neighbor Interatomic Distances  $r_{ij}$  and Partial Coordination Numbers  $N_{ij}$  in Rhombohedral GeTe, and FPMD and RMC Data for Liquid GeTe<sub>2</sub>

Ge–Te		Ge–Ge		Te–Te		$N_{\text{Ge-X}}$	$N_{\text{Te-X}}$
$r_{ij}$ (Å)	$N_{ij}$	$r_{ij}$ (Å)	$N_{ij}$	$r_{ij}$ (Å)	$N_{ij}$		
Rhombohedral GeTe <sup>20</sup>							
2.827 <sup>a</sup>	3.00 <sup>a</sup>					6.00	6.00
3.167 <sup>b</sup>	3.00 <sup>b</sup>						
Liquid GeTe <sub>2</sub> , FPMD Modeling (This Work)							
2.78(1)	2.08(10)	2.77(2)	0.74(20)	2.92(2)	1.28(34)	4.9(3)	3.4(4)
3.13(1)	2.12(10)						
Liquid GeTe <sub>2</sub> , RMC Modeling <sup>83</sup>							
2.81	4.1	2.9	0.6	2.81	0.8	4.7	2.9

<sup>a</sup>Short Ge–Te interatomic distances. <sup>b</sup>Long Ge–Te interatomic distances.

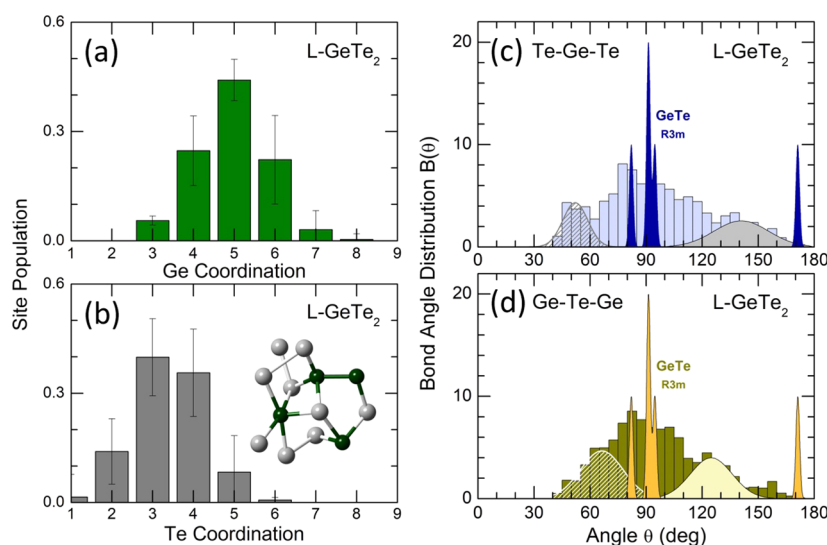


**Figure 9.** Local coordination and bond angles in liquid GeTe<sub>2</sub> at 1000 K derived using FPMD modeling with hybrid functional GGA/PBE0: coordination distributions around (a) central germanium and (b) central tellurium and bond angle distributions  $B(\theta)$  for (c) Te–Ge–Te and (d) Ge–Te–Ge triplets. The inset in (b) shows a typical structural motif in L-GeTe<sub>2</sub>. The angular distributions for rhombohedral GeTe are also shown in (c) and (d), including short (2.827 Å) and long (3.167 Å) Ge–Te interatomic distances. See the text for further details.

evolutionary relationship between crystalline GeTe with intrinsic Peierls distortion and metallic GeTe<sub>2</sub> liquid with reentrant Peierls distortion, reported earlier for molten GeTe.<sup>85</sup>

The integration of the  $g_{\text{GeGe}}(r)$  and  $g_{\text{TeTe}}(r)$  partial pair-distribution functions with a cutoff of 3.21 and 3.20 Å, respectively, corresponding to a well-defined minimum between the first and second neighbors in these two cases yields the partial coordination numbers  $N_{\text{Ge-Ge}} = 0.74 \pm 0.20$  and  $N_{\text{Te-Te}} = 1.28 \pm 0.34$  and the total Ge and Te local coordination  $N_{\text{Ge-X}} = N_{\text{Ge-Te}} + N_{\text{Ge-Ge}} = 4.9 \pm 0.3$  and  $N_{\text{Te-X}} = N_{\text{Te-Ge}} + N_{\text{Te-Te}} = 3.4 \pm 0.4$ ; Table 2. Consequently, liquid GeTe<sub>2</sub> is characterized by significantly higher local coordination numbers compared to g-GeTe<sub>2</sub>. The obtained FPMD results appear similar to those of RMC modeling,<sup>83</sup> except for two different Ge–Te NN distances in FPMD; Table 2.

The coordination distributions for germanium and tellurium in L-GeTe<sub>2</sub> are shown in Figure 9a,b. The Ge distribution is rather symmetric, centered at the average value  $\langle N_{\text{Ge-X}} \rangle = 5$ , and is spread over the  $3 \leq \langle N_{\text{Ge-X}} \rangle \leq 7$  range. The fraction of pure Ge–Te polyhedra is above 50%, the remaining mixed polyhedral species mostly contain 1 or 2 Ge–Ge homopolar bonds. The Te distribution is bimodal; the populations of three-fold and four-fold coordinated tellurium are comparable.

The Te local environment is essentially mixed, and the fraction of pure Te–Ge bonding in coordination polyhedra is below 27%. A fast dynamics of the local coordination changes, associated with a high fluidity of the metallic melt, reflected by the enhanced mean-square deviations of the derived parameters, and calculated over 1 ps of the simulation time, should also be noted.

The bond angle distributions of Te–Ge–Te and Ge–Te–Ge triplets are shown in Figure 9c,d. Both geometries of the Ge–Te polyhedra, revealed by the  $B_{\text{TeGeTe}}(\theta)$  angular dependence and polyhedral connectivity and reflected by the  $B_{\text{GeTeGe}}(\theta)$  function, are highly distorted. The corresponding  $B(\theta)$ s are spread over a wide angular range,  $40^\circ \leq \theta \leq 170^\circ$ , in comparison with the angular distributions for glassy GeTe<sub>2</sub>; Figure 3c,d. To some extent, the derived  $B_{\text{TeGeTe}}(\theta)$  and  $B_{\text{GeTeGe}}(\theta)$  functions are reminiscent of those in rhombohedral GeTe, although the degree of distortion in the metallic liquid appears to be considerably higher. In addition, intense contributions, centered at  $\theta(\text{TeGeTe}) \approx 52^\circ$  and  $\theta(\text{GeTeGe}) \approx 66^\circ$  (the crosshatched low- $\theta$  peaks in Figure 9c,d), are missing in Ge–Te crystals.

These low- $\theta$  features are indicative of a specific ring distribution  $R_c(p + q)$  in liquid GeTe<sub>2</sub> at 1000 K, Figure 10, consisting of a significant population of small rings,  $3 \leq p + q$

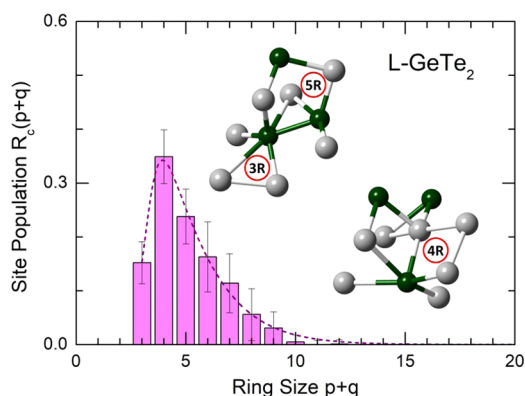


**Figure 10.** Ring population  $R_c(p+q)$  in liquid  $\text{GeTe}_2$  at 1000 K. The insets show characteristic structural motifs containing three-, four-, and five-fold rings. The dashed line representing the asymmetric shape of the ring distribution is a guide to the eye.

$\leq 7$ , and drastically different from  $R_c(p+q)$  in glassy  $\text{GeTe}_2$ ; Figure 5b. At the same time, similar ring distributions are observed in classical PCMs:  $\text{GeTe}$  or  $\text{GeTe-Sb}_2\text{Te}_3$ .<sup>86–88</sup>

In summary, we conclude that metallic  $\text{GeTe}_2$  liquid consists of  $\text{GeTe}$ -related modified structural fragments, including  $\text{Ge-Ge}$  bonds, coexisting with  $\text{Te-Te}$  dimers and  $\text{Te}_n$  oligomers. The connectivity analysis is presented in Figure S5. The distorted modified fragments appear to be more dense locally; the five-fold germanium coordination with longer  $\text{Ge-Te}$  NN distances is accompanied by shorter second neighbor separations, leaving rather intact more distant correlations. The higher fraction of  $\text{Ge-Ge}$  bonds in metallic  $\text{GeTe}_2$  liquid suggests a fast switching  $2\text{Ge-Te} = \text{Ge-Ge} + \text{Te-Te}$  in a highly fluid melt. The fraction of  $\text{Ge-Ge}$  bonds increases with temperature; Figure S6.

**$\text{GeTe}_2$  as a Precursor for the Next Generation of Phase-Change Materials.** The calculated electronic densities of states in glassy and liquid  $\text{GeTe}_2$  are consistent with the reported conductivity;<sup>23,78</sup> Figure 11. The band gap in g- $\text{GeTe}_2$  was found to be  $1.72 \pm 0.05$  eV compared to the experimental value of  $1.1 \pm 0.1$  eV. The PBE0 hybrid functional is known by overestimating the band gap.<sup>89</sup> A nearly

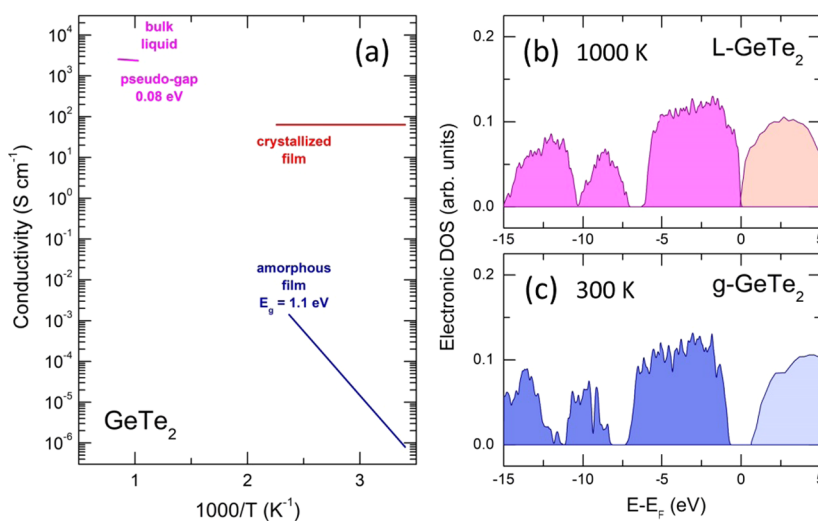


**Figure 11.** Electronic properties of  $\text{GeTe}_2$ : (a) experimental conductivity values for amorphous and crystallized  $\text{GeTe}_2$  thin films<sup>23</sup> and bulk liquid germanium ditelluride<sup>78</sup> and FPMD electronic density of states in (b) liquid and (c) glassy  $\text{GeTe}_2$  at 1000 and 300 K, respectively.

metallic conductivity in L- $\text{GeTe}_2$  in the vicinity of 1000 K with the apparent pseudogap of  $0.08 \pm 0.02$  eV is also reasonably reproduced by our FPMD simulations yielding the band gap of  $0.19 \pm 0.02$  eV, that is, by a factor of  $\approx 9$  lower than that in the glass. The metallic conductivity and low viscosity of molten  $\text{GeTe}_2$ , Figure 12, are a typical behavior of liquid phase-change

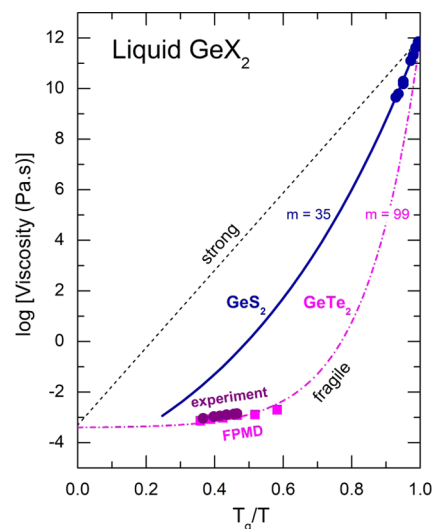


**Figure 12.** Angell plot for the temperature dependence of viscosity  $\eta(T)$  of  $\text{GeS}_2$  (blue) and  $\text{GeTe}_2$  (magenta): the experimental viscosity data<sup>78,98</sup> are shown by the solid circles, the high-temperature  $\eta(T)$  prediction for  $\text{GeS}_2$  is shown by the blue line,<sup>99</sup> and the FPMD viscosity calculated using the Stokes–Einstein relation (eq 4) is shown by the magenta squares (this work). The dashed-dotted line represents the MYEGA<sup>100</sup> viscosity (7) for  $\text{GeTe}_2$ . The derived fragility indices  $m$  are also shown. See the text for further details.

materials since high atomic mobility at elevated temperatures allows for rapid crystallization within the nanosecond range. On the other hand, the requested long-term data retention at ambient temperatures, which is critical for the reliable PCM operation, assumes a low-atomic-migration rate. Consequently, the viscosity–temperature dependence  $\eta(T)$  of the PCM liquids is characterized by a strong non-Arrhenius or fragile<sup>90</sup>

behavior with the fragility index  $m = \partial \log \eta / \partial (T_g/T) > 50$ .<sup>91</sup> The observed behavior provides fast diffusion at high temperatures with a sudden drop of diffusivity at lower temperatures. More recently, the high values of  $m \gtrsim 90$ <sup>92</sup> have been related to a fragile-to-strong<sup>93,94</sup> liquid–liquid transition on cooling and a breakdown<sup>95,96</sup> of the Stokes–Einstein relation

$$\eta(T) = \frac{k_B T}{6\pi D_{\text{eff}}(T) r_H} \quad (4)$$

between the viscosity  $\eta(T)$  and the effective atomic diffusion coefficient  $D_{\text{eff}}(T)$  at lower temperatures, approaching  $T_g$ ; where  $k_B$  is the Boltzmann constant,  $T$  is the absolute temperature, and  $r_H$  is the effective hydrodynamic radius. Experimental and computational verifications of this breakdown were obtained using quasi-elastic neutron scattering<sup>95,96</sup> and a neural network method in molecular dynamics.<sup>97</sup>

The mean-square displacements of Ge and Te in liquid GeTe<sub>2</sub>,  $\langle r_i^2(t) \rangle$ , Figure S7, were used for diffusion calculations

$$\langle r_i^2(t) \rangle = \left\langle \frac{1}{N_i} \left[ \sum_{i=1}^{N_i} [r_i(t) - r_i(0)]^2 \right] \right\rangle \quad (5)$$

where  $r_i(0)$  and  $r_i(t)$  are the positions of particle  $i$  for the initial time and time  $t$ , respectively,  $N_i$  is the total number of particles in the simulation box, and the angle brackets represent the average over initial times.

The germanium  $D_{\text{Ge}}$  and tellurium  $D_{\text{Te}}$  diffusion coefficients were derived from the respective  $\langle r_i^2(t) \rangle$  using the Einstein equation

$$D_i = \frac{1}{6} \lim_{t \rightarrow \infty} \frac{\partial \langle r_i^2(t) \rangle}{\partial t} \quad (6)$$

The derived  $D_{\text{Ge}}$  and  $D_{\text{Te}}$  are shown in Figure S8 and are similar to those in liquid GeTe.<sup>97</sup> The effective diffusion coefficient required for viscosity calculations was defined as  $D_{\text{eff}}(T) = 1/3D_{\text{Ge}}(T) + 2/3D_{\text{Te}}(T)$ .

Multiple approaches of the effective hydrodynamic radius  $r_H$  include the van der Waals radii,<sup>97</sup>  $r_{\text{vdW}}$ ; the Wigner–Seitz separation,<sup>101</sup>  $r_{\text{WS}}(T) = \sqrt[3]{(3/4\pi)V_m(T)N_A^{-1}}$ , where  $V_m(T)$  is the melt molar volume and  $N_A$  is the Avogadro constant; or the average half-size of the first coordination sphere,  $r_{\text{min}}/2$ , reflected by the first minimum  $r_{\text{min}}$  at the total or partial pair-distribution functions  $g_{ij}(r)$ ; Figure 8. Either of these approximations yields a rather narrow  $r_H$ -range,  $1.7 \text{ \AA} \leq r_H \leq 2.1 \text{ \AA}$ . We have used the experimental number density  $\rho_0(T)$ , eq 2, to calculate  $r_{\text{WS}}(T)$  and derive the FPMD viscosity  $\eta^{\text{FPMD}}(T)$ .

The calculated  $\eta^{\text{FPMD}}(T)$  values are visualized in Figure 12 plotted together with experimental viscosity<sup>78</sup> and the results for liquid GeS<sub>2</sub>.<sup>98,99</sup> We note a close similarity between the two data sets for GeTe<sub>2</sub>. The viscosity of germanium ditelluride is reminiscent of that for typical PCMs<sup>93,94,102</sup> and shows a high fragility index  $m = 99 \pm 5$ , which is found applying the Mauro–Yue–Ellison–Gupta–Allan (MYEGA) approach<sup>100</sup> based on the temperature dependence of configurational entropy and the experimental glass transition temperature for g-GeTe<sub>2</sub> ( $T_g = 466 \pm 3 \text{ K}$ , Figure S1)

$$\log \eta(T) = \log \eta_0 + [\log \eta(T_g) - \log \eta_0] \frac{T_g}{T} \exp \left[ \left( \frac{m}{\log \eta(T_g) - \log \eta_0} \right) \left( \frac{T_g}{T} - 1 \right) \right] \quad (7)$$

where  $\eta_0$  and  $\eta(T_g) = 10^{12} \text{ Pa}\cdot\text{s}$  are the viscosity values at  $T = \infty$  and  $T_g$ , respectively. In contrast, non-PCM germanium disulfide exhibits a modest fragility  $m = 35$ , typical for traditional chalcogenide glass-forming liquids.<sup>92,93</sup> In the used temperature range, 800–1300 K, we cannot observe a possible breakdown of the Stokes–Einstein relation (4), which probably occurs at lower temperatures.

The high electrical and optical contrast between glassy and crystalline states, fast atomic mobility in high-temperature liquid, and a strongly reduced diffusivity in the vicinity of  $T_g$  make GeTe<sub>2</sub> a promising precursor for the next generation of phase-change memories. A higher glass transition temperature, that is, 466 K vs 380 K for Ge<sub>2</sub>Sb<sub>2</sub>Te<sub>5</sub> or Ag–In–Sb–Te,<sup>93,94</sup> suggests better data retention at ambient temperatures and more reliable nonvolatile memory operation. The thermodynamic metastability of GeTe<sub>2</sub> and the disproportionation reaction  $\text{GeTe}_2 \rightleftharpoons \text{GeTe} + \text{Te}$  observed in the bulk metallic melt could certainly affect the fast transformation rate. Nevertheless, all ternary compounds along the GeTe–Sb<sub>2</sub>Te<sub>3</sub> composition line,<sup>103</sup> including Ge<sub>2</sub>Sb<sub>2</sub>Te<sub>5</sub>,<sup>104</sup> exhibit incongruent melting and hence a dissociation into GeTe and Sb<sub>2</sub>Te<sub>3</sub> end-members in the melt.<sup>105</sup> Consequently, the bulk metastability is not necessarily an invincible obstacle for fast transformers. Besides, we cannot exclude that stability and kinetic criteria could be different for macroscopic bulk and nanometer spots in a PCM thin layer.

Another possible complication includes a tetrahedral interconnected subnetwork in glassy GeTe<sub>2</sub> with intermediate-range ordering reminiscent of g-GeS<sub>2</sub> and g-GeSe<sub>2</sub>. However, metal doping, e.g., using silver or copper, leads to network depolymerization<sup>106,107</sup> and faster transformation processes in the amorphous state. Copper tellurogermanate Cu<sub>2</sub>GeTe<sub>3</sub> is an exciting example revealing new perspectives.<sup>108,109</sup> We should note that a significant population of triangular rings in Cu<sub>2</sub>GeTe<sub>3</sub> are also present in liquid GeTe<sub>2</sub>, Figure 10, revealing a resemblance in intermediate-range structures. Atomic layer deposition of GeTe<sub>2</sub>–Sb<sub>2</sub>Te<sub>3</sub> thin films<sup>110,111</sup> offers additional horizons for nanoscale phase-change random-access memory based on germanium ditelluride.<sup>112</sup>

## CONCLUSIONS

A missing member of the tetrahedral GeX<sub>2</sub> glass family, bulk glassy GeTe<sub>2</sub>, was obtained using a specially designed quenching procedure in silica capillaries and was studied using high-energy X-ray diffraction and Raman scattering supported by first-principles simulations. In contrast to canonical GeS<sub>2</sub> and GeSe<sub>2</sub> vitreous alloys, bulk g-GeTe<sub>2</sub> represents a nearly equimolar mixture of tetrahedral GeTe<sub>4</sub> and trigonal GeTe<sub>3</sub> units coexisting with Te–Te dimers and Te<sub>*n*</sub> oligomers,  $n \leq 10$ , and a small fraction of Ge–Ge dimers (3.6% of Ge–Ge vs 26.3% of Te–Te homopolar bonds). In addition, 31% of tellurium was found to be three-fold coordinated. These experimental diffraction data and simulation results using the first-principles molecular dynamics with a hybrid exchange–correlation functional PBE0 and van der

Waals dispersion corrections are confirmed by independent vibrational studies and DFT modeling of the Raman spectra. The  $A_1$  symmetric in-phase breathing of corner-sharing  $\text{GeTe}_4$  tetrahedra at  $130\text{ cm}^{-1}$  and multiple contributions to a broad unresolved  $160\text{ cm}^{-1}$  mode, consisting of Te–Te stretching and symmetric Ge–Te breathing in trigonal  $\text{GeTe}_3$  pyramids and edge-sharing  $\text{GeTe}_4$  units, are the main vibrational features. A dominant role of the Te–Te stretching was verified by the increasing amplitude of the  $160\text{ cm}^{-1}$  mode in bulk  $\text{Ge}_x\text{Te}_{1-x}$  glasses in the range of  $0.1 \leq x \leq 0.25$ . A complex structural and bonding pattern in bulk glassy  $\text{GeTe}_2$  is related to the thermodynamic metastability and a dissociation reaction  $\text{GeTe}_2 \rightleftharpoons \text{GeTe} + \text{Te}$ .

A dramatic difference was also found between  $\text{GeTe}_2$  and  $\text{GeS}_2/\text{GeSe}_2$  melts. Just above liquidus, the available diffraction data, conductivity, and viscosity results show that  $\text{GeTe}_2$  becomes a dense metallic liquid. Our FPMD simulations reproduce well both the neutron diffraction results, electronic properties and atomic dynamics. Liquid  $\text{GeTe}_2$  appears to be highly coordinated with the average germanium coordination number  $\langle N_{\text{Ge}-x} \rangle = 4.9 \pm 0.3$  and high tellurium coordination  $\langle N_{\text{Te}-x} \rangle = 3.4 \pm 0.4$ , where X = Ge and/or Te. The Ge–Te NN interatomic distances exhibit a strong Peierls distortion (two equally populated separations at 2.78 and 3.13 Å), which are substantially longer than the Ge–Te distance at 2.62 Å in the glass. The first and second neighbor correlations overlap in contrast to well-separated nearest and next-nearest neighbors in g- $\text{GeTe}_2$ . Locally dense GeTe-related structural fragments are also characterized by fast switching  $2\text{Ge}-\text{Te} = \text{Ge}-\text{Ge} + \text{Te}-\text{Te}$ , increasing with temperature. On the contrary, molten  $\text{GeS}_2$  and  $\text{GeSe}_2$  remain tetrahedral and semiconducting.

The reported semiconducting nature of amorphous  $\text{GeTe}_2$  thin films was also reflected by the FPMD results. The calculated band gap appears to be  $1.72 \pm 0.05\text{ eV}$  in comparison with experimental  $E_g = 1.1 \pm 0.1\text{ eV}$ . The conductivity of metallic liquid  $\text{GeTe}_2$  shows a pseudogap of  $0.08 \pm 0.02\text{ eV}$ , while the FPMD simulations reveal a band gap of  $0.19 \pm 0.02\text{ eV}$  (the PBE0 hybrid functional is known by slightly overestimating the band gap). The low viscosity of liquid  $\text{GeTe}_2$  was consistently reproduced by the first-principles calculations yielding a high fragility index  $m = 99 \pm 5$  and a presumably fast transformation rate at high temperatures combined with low atomic mobility close to or below glass transition temperature  $T_g$ , favorable for reliable long-term data retention in nonvolatile memories. The observed and predicted characteristic features make  $\text{GeTe}_2$  a promising precursor for the next generation of phase-change materials, especially coupled with additional metal doping, depolymerizing the tetrahedral interconnected glass network and accelerating (sub)nanosecond crystallization.

## ■ ASSOCIATED CONTENT

### SI Supporting Information

The Supporting Information is available free of charge at <https://pubs.acs.org/doi/10.1021/acs.chemmater.0c04409>.

DSC traces of selected Ge–Te bulk glasses and the compositional dependence of the glass transition temperature; typical examples of the obtained bulk glassy  $\text{GeTe}_2$ ; experimental and derived FPMD interference functions for glassy  $\text{GeTe}_2$ ; partial structure factors for Ge–Ge, Ge–Te, and Te–Te atomic pairs; tetrahedral orientational order parameter  $q$  for  $\text{GeTe}_4$

polyhedra in bulk glassy  $\text{GeTe}_2$ ; optimized DFT cluster ETH- $\text{Ge}_2\text{Te}_6$  and derived DFT Raman spectrum; size of  $\text{Te}_n$  and  $\text{Ge}_n$  oligomers in liquid  $\text{GeTe}_2$  at 1000 K; fraction of Ge–Ge homopolar bonds in glassy, supercooled, and liquid  $\text{GeTe}_2$  as a function of temperature; germanium and tellurium mean-square displacements in liquid  $\text{GeTe}_2$  at 800 and 1300 K; germanium and tellurium diffusion coefficients in liquid  $\text{GeTe}_2$ ; and optimized geometry parameters of size-limited Ge–Te clusters used in DFT modeling of vibrational properties (PDF)

## ■ AUTHOR INFORMATION

### Corresponding Author

Eugene Bychkov – *Laboratoire de Physico-Chimie de l'Atmosphère, Université du Littoral Côte d'Opale, 59140 Dunkerque, France; ILIT RAS–Branch of the FSRC "Crystallography and Photonics" RAS, 140700 Shatura, Moscow Region, Russia; [orcid.org/0000-0002-3292-1205](https://orcid.org/0000-0002-3292-1205); Phone: +33 328 658250; Email: [Eugene.Bychkov@univ-littoral.fr](mailto:Eugene.Bychkov@univ-littoral.fr); Fax: +33 328 658244*

### Authors

Andrey Tverjanovich – *Institute of Chemistry, St. Petersburg State University, 198504 St. Petersburg, Russia*

Maxim Khomenko – *ILIT RAS–Branch of the FSRC "Crystallography and Photonics" RAS, 140700 Shatura, Moscow Region, Russia*

Chris J. Benmore – *X-ray Science Division, Advanced Photon Source, Argonne National Laboratory, Argonne, Illinois 60439, United States; [orcid.org/0000-0001-7007-7749](https://orcid.org/0000-0001-7007-7749)*

Maria Bokova – *Laboratoire de Physico-Chimie de l'Atmosphère, Université du Littoral Côte d'Opale, 59140 Dunkerque, France*

Anton Sokolov – *Laboratoire de Physico-Chimie de l'Atmosphère, Université du Littoral Côte d'Opale, 59140 Dunkerque, France*

Daniele Fontanari – *Laboratoire de Physico-Chimie de l'Atmosphère, Université du Littoral Côte d'Opale, 59140 Dunkerque, France*

Mohammad Kassem – *Laboratoire de Physico-Chimie de l'Atmosphère, Université du Littoral Côte d'Opale, 59140 Dunkerque, France; [orcid.org/0000-0003-0512-0004](https://orcid.org/0000-0003-0512-0004)*

Takeshi Usuki – *Faculty of Science, Yamagata University, Yamagata 990-8560, Japan*

Complete contact information is available at: <https://pubs.acs.org/doi/10.1021/acs.chemmater.0c04409>

### Author Contributions

The manuscript was written through the contributions of all authors. All authors have given approval to the final version of the manuscript.

### Notes

The authors declare no competing financial interest.

## ■ ACKNOWLEDGMENTS

This work was supported by the Ministry of Science and Higher Education under agreement 075-15-2019-1950, state assignment FSRC "Crystallography and Photonics", Russian Academy of Sciences. Work at the Advanced Photon Source, Argonne National Laboratory, was supported in part by the Office of Basic Energy Sciences, US Department of Energy,

under Contract No. DE-AC02-06CH1135. The DSC measurements in part were carried out in the resource center of St. Petersburg State University, "Thermogravimetric and Calorimetric Research Center". The FPMD simulations were carried out using the HPC computing resources at Lomonosov Moscow State University and at the ILIT RAS in Shatura (Moscow Region). This work was also granted access to the HPC resources of IDRIS (France) under the allocation 2019-A0070910639 made by Grand Equipement National de Calcul Intensif (GENCI) and to use the CALCULCO computing platform, supported by Service COmmun du Système d'Information de l'Université du Littoral Côte d'Opale (SCoSI/ULCO).

## REFERENCES

- (1) Susman, S.; Volin, K. J.; Montague, D. G.; Price, D. L. The Structure of Vitreous and Liquid GeSe<sub>2</sub>: a Neutron Diffraction Study. *J. Non-Cryst. Solids* **1990**, *125*, 168–180.
- (2) Petri, I.; Salmon, P. S.; Fischer, H. E. Defects in a Disordered World: The Structure of Glassy GeSe<sub>2</sub>. *Phys. Rev. Lett.* **2000**, *84*, No. 2413.
- (3) Bytchkov, A.; Cuello, G. J.; Kohara, S.; Benmore, C. J.; Price, D. L.; Bychkov, E. Unraveling the Atomic Structure of Ge-Rich Sulfide Glasses. *Phys. Chem. Chem. Phys.* **2013**, *15*, 8487–8494.
- (4) Blaineau, S.; Jund, P.; Drabold, D. A. Physical Properties of a GeS<sub>2</sub> Glass using Approximate ab initio Molecular Dynamics. *Phys. Rev. B* **2003**, *67*, No. 094204.
- (5) Giacomazzi, L.; Massobrio, C.; Pasquarello, A. First-Principles Investigation of the Structural and Vibrational Properties of Vitreous GeSe<sub>2</sub>. *Phys. Rev. B* **2007**, *75*, No. 174207.
- (6) Celino, M.; Le Roux, S.; Ori, G.; Coasne, B.; Bouzid, A.; Boero, M.; Massobrio, C. First-Principles Molecular Dynamics Study of Glassy GeS<sub>2</sub>: Atomic Structure and Bonding Properties. *Phys. Rev. B* **2013**, *88*, No. 174201.
- (7) Dittmar, G.; Schäfer, H. Die Kristallstruktur von HT-GeS<sub>2</sub>. *Acta Crystallogr., Sect. B* **1975**, *31*, 2060–2064.
- (8) Dittmar, G.; Schäfer, H. Die Kristallstruktur von Germaniumdiselelenid. *Acta Crystallogr., Sect. B* **1976**, *32*, 2726–2728.
- (9) Dittmar, G.; Schäfer, H. Die Kristallstruktur von LT-GeS<sub>2</sub>. *Acta Crystallogr., Sect. B* **1976**, *32*, 1188–1192.
- (10) Grzechnik, A.; Stolen, S.; Bakken, E.; Grande, T.; Mezouar, M. Structural Transformations in Three-Dimensional Crystalline GeS<sub>2</sub> at High Pressures and High Temperatures. *J. Solid State Chem.* **2000**, *150*, 121–127.
- (11) Viaene, W.; Moh, G. H. Das binäre System Germanium–Schwefel und p–T–Relationen im Druckbereich bis 5 kb. *Neues Jahrb. Mineral., Abh.* **1973**, *119*, 113–144.
- (12) Ross, L.; Bourgon, M. Germanium-selenium phase diagram. *Can. J. Chem.* **1969**, *47*, 2555–2559.
- (13) Maruyama, K.; Ebata, H.; Suzuki, S.; Misawa, M.; Takeda, S.; Kawakita, Y. Structural Studies on Liquid Ge–Chalcogen Mixtures by using Neutron Diffraction. *J. Non-Cryst. Solids* **1999**, *250–252*, 483–487.
- (14) McHugh, J. P.; Tiller, W. A. Germanium-tellurium phase diagram in the vicinity of the compound GeTe. *Trans. Met. Soc. AIME* **1960**, *218*, 187–188.
- (15) Schlieper, A.; Feutalais, Y.; Fries, S. G.; Legendre, B.; Blachnik, R. Thermodynamic Evaluation of the Germanium–Tellurium System. *CALPHAD* **1999**, *23*, 1–18.
- (16) Wuttig, M.; Yamada, N. Phase-Change Materials for Rewritable Data Storage. *Nat. Mater.* **2007**, *6*, 824–832.
- (17) Kolobov, A. V.; Tominaga, J. *Chalcogenides: Metastability and Phase Change Phenomena*; Springer: Berlin, 2012; pp 149–216.
- (18) Ríos, C.; Stegmaier, M.; Hosseini, P.; Wang, D.; Scherer, T.; Wright, C. D.; Bhaskaran, H.; Pernice, W. H. P. Integrated All-Photonic Non-Volatile Multi-Level Memory. *Nat. Photonics* **2015**, *9*, 725–732.
- (19) Zhang, W.; Mazzarello, R.; Wuttig, M.; Ma, E. Designing Crystallization in Phase-Change Materials for Universal Memory and Neuro-Inspired Computing. *Nat. Rev. Mater.* **2019**, *4*, 150–168.
- (20) Serrano-Sánchez, F.; Funes, M.; Nemes, N. M.; Dura, O. J.; Martínez, J. L.; Prado-Gonjal, J.; Fernández-Díaz, M. T.; Alonso, J. A. Low Lattice Thermal Conductivity in Arc-Melted GeTe with Ge-Deficient Crystal Structure. *Appl. Phys. Lett.* **2018**, *113*, No. 083902.
- (21) Bienenstock, A. Threefold Coordinated Model Structure of Amorphous GeS, GeSe and GeTe. *J. Non-Cryst. Solids* **1973**, *11*, 447–458.
- (22) Tsunetomo, K.; Sugishima, T.; Imura, T.; Osaka, Y. Stability of Metastable GeTe<sub>2</sub> in Thin Films. *J. Non-Cryst. Solids* **1987**, *95–96*, 509–516.
- (23) Fukumoto, H.; Tsunetomo, K.; Imura, T.; Osaka, Y. Structural Changes of Amorphous GeTe<sub>2</sub> Films by Annealing (Formation of Metastable Crystalline GeTe<sub>2</sub> Films). *J. Phys. Soc. Jpn.* **1987**, *56*, 158–162.
- (24) DeNeufville, J. P. Chemical Aspects of Glass Formation in Telluride Systems. *J. Non-Cryst. Solids* **1972**, *8–10*, 85–105.
- (25) Fee, M. G.; Trodahl, H. J. Bonding and Short Range Order in a-Ge<sub>x</sub>Te<sub>1-x</sub> Alloys. In *Disordered Semiconductors*; Kastner, M. A.; Thomas, G. A.; Ovshinsky, S. R., Eds.; Plenum: New York, 1987; pp 307–315.
- (26) Jovári, P.; Piarristeguy, A.; Escalier, R.; Kaban, I.; Bednarčík, J.; Pradel, A. Short Range Order and Stability of Amorphous Ge<sub>x</sub>Te<sub>100-x</sub> Alloys (12 ≤ x ≤ 44.6). *J. Phys.: Condens. Matter* **2013**, *25*, No. 195401.
- (27) Hammersley, A. P.; Svensson, S. O.; Hanfland, M.; Fitch, A. N.; Häusermann, D. Two-Dimensional Detector Software: From Real Detector to Idealised Image or Two-Theta Scan. *High Pressure Res.* **1996**, *14*, 235–248.
- (28) Skinner, L. B.; Benmore, C. J.; Parise, J. B. Area Detector Corrections for High Quality Synchrotron X-ray Structure Factor Measurements. *Nucl. Instrum. Methods Phys. Res., Sect. A* **2012**, *662*, 61–70.
- (29) Hutter, J.; Iannuzzi, M.; Schimann, F.; VandeVondele, J. CP2K: Atomistic Simulations of Condensed Matter Systems. *Wiley Interdiscip. Rev.: Comput. Mol. Sci.* **2014**, *4*, 15–25.
- (30) Perdew, J. P.; Ernzerhof, M.; Burke, K. Rationale for Mixing Exact Exchange with Density Functional Approximations. *J. Chem. Phys.* **1996**, *105*, 9982–9985.
- (31) Adamo, C.; Barone, V. Toward Reliable Density Functional Methods without Adjustable Parameters: the PBE0 Model. *J. Chem. Phys.* **1999**, *110*, 6158–6170.
- (32) Grimme, S.; Ehrlich, S.; Goerigk, L. Effect of the Damping Function in Dispersion Corrected Density Functional Theory. *J. Comput. Chem.* **2011**, *32*, 1456–1465.
- (33) Micoulaut, M. Communication: Van der Waals Corrections for an Improved Structural Description of Telluride Based Materials. *J. Chem. Phys.* **2013**, *138*, No. 061103.
- (34) Bouzid, A.; Massobrio, C.; Boero, M.; Ori, G.; Sykina, K.; Furet, E. Role of the van der Waals Interactions and Impact of the Exchange-Correlation Functional in Determining the Structure of Glassy GeTe<sub>4</sub>. *Phys. Rev. B* **2015**, *92*, No. 134208.
- (35) Akola, J.; Jones, R. O.; Kohara, S.; Kimura, S.; Kobayashi, K.; Takata, M.; Matsunaga, T.; Kojima, R.; Yamada, N. Experimentally Constrained Density-Functional Calculations of the Amorphous Structure of the Prototypical Phase-Change Material Ge<sub>2</sub>Sb<sub>2</sub>Te<sub>5</sub>. *Phys. Rev. B* **2009**, *80*, No. 020201.
- (36) Matsunaga, T.; Akola, J.; Kohara, S.; Honma, T.; Kobayashi, K.; Ikenaga, E.; Jones, R. O.; Yamada, N.; Takata, M.; Kojima, R. From Local Structure to Nanosecond Recrystallization Dynamics in AgInSbTe Phase-Change Materials. *Nat. Mater.* **2011**, *10*, 129–134.
- (37) Gereben, O.; Pusztai, L. RMC\_POT, a Computer Code for Reverse Monte Carlo Modeling the Structure of Disordered Systems Containing Molecules of Arbitrary Complexity. *J. Comput. Chem.* **2012**, *33*, 2285–2291.

- (38) Hartwigsen, C.; Goedecker, S.; Hutter, J. Relativistic Separable Dual-Space Gaussian Pseudo-potentials from H to Rn. *Phys. Rev. B* **1998**, *58*, No. 3641.
- (39) Nosé, S. A Molecular Dynamics Method for Simulations in the Canonical Ensemble. *Mol. Phys.* **1984**, *52*, 255–268.
- (40) Hoover, W. G. Canonical Dynamics: Equilibrium Phase-Space Distributions. *Phys. Rev. A* **1985**, *31*, No. 1695.
- (41) Le Roux, S.; Jund, P. Ring Statistics Analysis of Topological Networks: New Approach and Application to Amorphous GeS<sub>2</sub> and SiO<sub>2</sub> Systems. *Comput. Mater. Sci.* **2010**, *49*, 70–83.
- (42) Kohara, S.; Ohno, H.; Tabaka, M.; Usuki, T.; Morita, H.; Suzuya, K.; Akola, J.; Pusztai, L. Lead Silicate Glasses: Binary Network-Former Glasses with Large Amounts of Free Volume. *Phys. Rev. B* **2010**, *82*, No. 134209.
- (43) Heimbach, I.; Rhiem, F.; Beule, F.; Knodt, D.; Heinen, J.; Jones, R. O. pyMolDyn: Identification, Structure, and Properties of Cavities/Vacancies in Condensed Matter and Molecules. *J. Comput. Chem.* **2017**, *38*, 389–394.
- (44) Frisch, M. J.; Trucks, G. W.; Schlegel, H. B.; Scuseria, G. E.; Robb, M. A.; Cheeseman, J. R.; Scalmani, G.; Barone, V.; Mennucci, B.; Petersson, G. A. et al. *Gaussian 16*, revision B.01; Gaussian, Inc.: Wallingford, CT, 2016.
- (45) Becke, A. D. Density-Functional Thermochemistry. III. The Role of Exact Exchange. *J. Chem. Phys.* **1993**, *98*, 5648–5653.
- (46) Lee, C.; Yang, W.; Parr, R. G. Development of the Colle-Salvetti Correlation-Energy Formula into a Functional of the Electron Density. *Phys. Rev. B* **1988**, *37*, No. 785.
- (47) Feller, D. The Role of Databases in Support of Computational Chemistry Calculations. *J. Comput. Chem.* **1996**, *17*, 1571–1586.
- (48) Peterson, K. A.; Figgen, D.; Goll, E.; Stoll, H.; Dolg, M. Systematically Convergent Basis Sets with Relativistic Pseudopotentials. II. Small-Core Pseudopotentials and Correlation Consistent Basis Sets for the Post-d Group 16–18 Elements. *J. Chem. Phys.* **2003**, *119*, 11113–11123.
- (49) Bacskey, G. B. A Quadratically Convergent Hartree-Fock (QC-SCF) Method. Application to Closed Shell Systems. *Chem. Phys.* **1981**, *61*, 385–404.
- (50) Cuisset, A.; Hindle, F.; Laureyns, J.; Bychkov, E. Structural Analysis of xCsCl(1-x)Ga<sub>2</sub>S<sub>3</sub> Glasses by Means of DFT Calculations and Raman Spectroscopy. *J. Raman Spectrosc.* **2010**, *41*, 1050–1058.
- (51) Kassem, M.; Khaoulani, S.; Cuisset, A.; Le Coq, D.; Masselin, P.; Bychkov, E. Mercury Thioarsenate Glasses: a Hybrid Chain/Pyramidal Network. *RSC Adv.* **2014**, *4*, 49236–49246.
- (52) Tverjanovich, A.; Cuisset, A.; Fontanari, D.; Bychkov, E. Structure of Se-Te Glasses by Raman Spectroscopy and DFT Modelling. *J. Am. Ceram. Soc.* **2018**, *101*, 5188–5197.
- (53) Bychkov, E.; Benmore, C. J.; Price, D. L. Compositional Changes of the First Sharp Diffraction Peak in Binary Selenide Glasses. *Phys. Rev. B* **2005**, *72*, No. 172107.
- (54) Hosokawa, S.; Pilgrim, W.-C.; Bézar, J.-F.; Kohara, S. Anomalous X-ray Scattering Studies on Semiconducting and Metallic Glasses. *Eur. Phys. J.: Spec. Top.* **2012**, *208*, 291–304.
- (55) Benmore, C. J.; Hart, R. T.; Mei, Q.; Price, D. L.; Yarger, J.; Tulk, C. A.; Klug, D. D. Intermediate Range Chemical Ordering in Amorphous and Liquid Water, Si, and Ge. *Phys. Rev. B* **2005**, *72*, No. 132201.
- (56) Salmon, P. S.; Martin, R. A.; Mason, P. E.; Cuello, G. J. Topological versus Chemical Ordering in Network Glasses at Intermediate and Extended Length Scales. *Nature* **2005**, *435*, 75–78.
- (57) Mei, Q.; Benmore, C. J.; Hart, R. T.; Bychkov, E.; Salmon, P. S.; Martin, C. D.; Michel, F. M.; Antao, S. M.; Chupas, P. J.; Lee, P. L.; Shastri, S. D.; Parise, J. B.; Leinenweber, K.; Amin, S.; Yarger, J. L. Topological Changes in Glassy GeSe<sub>2</sub> at Pressures up to 9.3 GPa Determined by High-Energy X-ray and Neutron Diffraction Measurements. *Phys. Rev. B* **2006**, *74*, No. 014203.
- (58) Soignard, E.; Tsiok, O. B.; Tverjanovich, A. S.; Bychkov, A.; Sokolov, A.; Brazhkin, V. V.; Benmore, C. J.; Bychkov, E. Pressure-Driven Chemical Disorder in Glassy As<sub>2</sub>S<sub>3</sub> up to 14.7 GPa, Postdensification Effects, and Applications in Materials Design. *J. Phys. Chem. B* **2020**, *124*, 430–442.
- (59) Cherin, P.; Unger, P. Two-Dimensional Refinement of the Crystal Structure of Tellurium. *Acta Crystallogr.* **1967**, *23*, 670–671.
- (60) Chau, P.-L.; Hardwick, A. J. A New Order Parameter for Tetrahedral Configurations. *Mol. Phys.* **1998**, *93*, 511–518.
- (61) Errington, J. R.; Debenedetti, P. G. Relationship between Structural Order and the Anomalies of Liquid Water. *Nature* **2001**, *409*, 318–321.
- (62) Wiedemeier, H.; von Schnering, H. G. Refinement of the Structures of GeS, GeSe, SnS and SnSe. *Z. Kristallgr.* **1978**, *148*, 295–303.
- (63) Akola, J.; Jones, R. O. Binary Alloys of Ge and Te: Order, Voids, and the Eutectic Composition. *Phys. Rev. Lett.* **2008**, *100*, No. 205502.
- (64) Pethes, I.; Piarristeguy, A.; Pradel, A.; Michalik, S.; Nemausat, R.; Darpentigny, J.; Jóvári, P. Short Range Order and Topology of Ge<sub>x</sub>Ga<sub>x</sub>Te<sub>100-2x</sub> glasses. *J. Alloys Compd.* **2020**, *834*, No. 155097.
- (65) Grimme, S.; Antony, J.; Ehrlich, S.; Krieg, H. A Consistent and Accurate ab initio Parametrization of Density Functional Dispersion Correction (DFT-D) for the 94 Elements H-Pu. *J. Chem. Phys.* **2010**, *132*, No. 154104.
- (66) Kalikka, J.; Akola, J.; Jones, R. O.; Kohara, S.; Usuki, T. Amorphous Ge<sub>15</sub>Te<sub>85</sub>: Density Functional, High-Energy X-ray and Neutron Diffraction Study. *J. Phys.: Condens. Matter* **2012**, *24*, No. 015802.
- (67) Becke, A. D. Density-Functional Exchange-Energy Approximation with Correct Asymptotic Behavior. *Phys. Rev. A* **1988**, *38*, No. 3098.
- (68) Lee, C.; Yang, W.; Parr, R. G. Development of the Colle-Salvetti correlation-energy formula into a functional of the electron density. *Phys. Rev. B* **1988**, *37*, No. 785.
- (69) Fisher, G. B. Bonding in Non-Tetrahedrally Coordinated Amorphous Solids. In *Physics of Structurally Disordered Solids*; Mitra, S. S., Ed.; Springer: Boston, MA, 1976; pp 703–737.
- (70) Némec, P.; Nazabal, V.; Dussauze, M.; Ma, H.-L.; Bouyrie, Y.; Zhang, X.-H. Ga-Ge-Te Amorphous Thin Films Fabricated by Pulsed Laser Deposition. *Thin Solid Films* **2013**, *531*, 454–459.
- (71) Chen, Y.; Wang, R.; Shen, X.; Xu, T. Multiple singularities of optical properties in Ge<sub>x</sub>Te<sub>100-x</sub> films. *Infrared Phys. Technol.* **2020**, *106*, No. 103280.
- (72) Voleská, L.; Akola, J.; Jóvári, P.; Gutwirth, J.; Wágner, T.; Vasileiadis, Th.; Yannopoulos, S. N.; Jones, R. O. Structure, Electronic, and Vibrational Properties of Glassy Ga<sub>11</sub>Ge<sub>11</sub>Te<sub>78</sub>: Experimentally Constrained Density Functional Study. *Phys. Rev. B* **2012**, *86*, No. 094108.
- (73) Blaineau, S.; Jund, P. Vibrational Signature of Broken Chemical Order in a GeS<sub>2</sub> Glass: A Molecular Dynamics Simulation. *Phys. Rev. B* **2004**, *69*, No. 064201.
- (74) Masselin, P.; Le Coq, D.; Cuisset, A.; Bychkov, E. Spatially Resolved Raman Analysis of Laser Induced Refractive Index Variation in Chalcogenide Glass. *Opt. Mater. Express* **2012**, *2*, 1768–1775.
- (75) Gourvest, E.; Lhostis, S.; Kreisel, J.; Armand, M.; Maitrejean, S.; Roule, A.; Vallée, C. Evidence of Germanium Precipitation in Phase-Change Ge<sub>1-x</sub>Te<sub>x</sub> Thin Films by Raman Scattering. *Appl. Phys. Lett.* **2009**, *95*, No. 031908.
- (76) Raty, J. Y.; Zhang, W.; Lucas, J.; Chen, C.; Mazzarello, R.; Bichara, C.; Wuttig, M. Aging Mechanisms in Amorphous Phase-Change Materials. *Nat. Commun.* **2015**, *6*, No. 7467.
- (77) Gabardi, S.; Caravati, S.; Sosso, G. C.; Behler, J.; Bernasconi, M. Microscopic Origin of Resistance Drift in the Amorphous State of the Phase-Change Compound GeTe. *Phys. Rev. B* **2015**, *92*, No. 054201.
- (78) Glazov, V. M.; Chizhevskaya, S. N.; Glagoleva, N. N. *Liquid Semiconductors (Zhidkie Poluprovodniki)*; Nauka: Moscow, 1967; p 198.
- (79) Krebs, H.; Fischer, P. Electrical Conductivity of Melts and their Ability to Form Glasses in the System Ge+As+Te. *Discuss. Faraday Soc.* **1970**, *50*, 35–44.

- (80) Tsuchiya, Y.; Saitoh, H. Semiconductor-Metal Transition Induced by the Structural Transition in Liquid  $\text{Ge}_{15}\text{Te}_{85}$ . *J. Phys. Soc. Jpn.* **1993**, *62*, 1272–1278.
- (81) Wei, S.; Coleman, G. J.; Lucas, P.; Angell, C. A. Glass Transitions, Semiconductor-Metal Transitions, and Fragilities in Ge-V-Te (V = As, Sb) Liquid Alloys: The Difference One Element Can Make. *Phys. Rev. Appl.* **2017**, *7*, No. 034035.
- (82) Kameda, Y.; Uemura, O.; Usuki, T. Time-of-Flight Neutron Diffraction Study of Amorphous and Liquid Ge-Te Alloys. *Mater. Trans. JIM* **1996**, *37*, 1655–1658.
- (83) Kaban, I.; J v ri, P.; Hoyer, W.; Delaplane, R. G.; Wannberg, A. Structural Studies on Te-rich Ge-Te Melts. *J. Phys.: Condens. Matter* **2006**, *18*, 2749–2760.
- (84) Tsuchiya, Y. The Anomalous Negative Thermal Expansion Coefficient and the Compressibility Maximum of Molten Ge-Te Alloys. *J. Phys. Soc. Jpn.* **1991**, *60*, 227–234.
- (85) Raty, J. Y.; Godlevsky, V.; Ghosez, P.; Bichara, C.; Gaspard, J. P.; Chelikowsky, J. R. Evidence of a Reentrant Peierls Distortion in Liquid GeTe. *Phys. Rev. Lett.* **2000**, *85*, No. 1950.
- (86) Kohara, S.; Kato, K.; Kimura, S.; Tanaka, H.; Usuki, T.; Suzuya, K.; Tanaka, H.; Moritomo, Y.; Matsunaga, T.; Yamada, N.; Tanaka, Y.; Suematsu, H.; Takata, M. Structural Basis for the Fast Phase Change of  $\text{Ge}_2\text{Sb}_2\text{Te}_5$ : Ring Statistics Analogy between the Crystal and Amorphous States. *Appl. Phys. Lett.* **2006**, *89*, No. 201910.
- (87) Flores-Ruiz, H.; Micoulaut, M.; Coulet, M.-V.; Piarristeguy, A. A.; Johnson, M. R.; Cuello, G. J.; Pradel, A. Effect of Tellurium Concentration on the Structural and Vibrational Properties of Phase-Change Ge-Sb-Te Liquids. *Phys. Rev. B* **2015**, *92*, No. 134205.
- (88) Schumacher, M.; Weber, H.; J v ri, P.; Tsuchiya, Y.; Youngs, T. G. A.; Kaban, I.; Mazzarello, R. Structural, Electronic and Kinetic Properties of the Phase-Change Material  $\text{Ge}_2\text{Sb}_2\text{Te}_5$  in the Liquid State. *Sci. Rep.* **2016**, *6*, No. 27434.
- (89) Song, J.-W.; Giorgi, G.; Yamashita, K.; Hirao, K. Singularity-Free Hybrid Functional with a Gaussian-Attenuating Exact Exchange in a Plane-Wave Basis. *J. Chem. Phys.* **2013**, *138*, No. 241101.
- (90) Angell, C. A. Formation of Glasses from Liquids and Biopolymers. *Science* **1995**, *267*, 1924–1935.
- (91) Neumann, H.; Herwig, F.; Hoyer, H. The Short Range Order of Liquid Eutectic  $\text{A}_{III}\text{-Te}$  and  $\text{A}_{IV}\text{-Te}$  Alloys. *J. Non-Cryst. Solids* **1996**, *205–207*, 438–442.
- (92) Orava, J.; Greer, L.; Gholipour, B.; Hewak, D. W.; Smith, C. E. Characterization of Supercooled Liquid  $\text{Ge}_2\text{Sb}_2\text{Te}_5$  and its Crystallization by Ultrafast-Heating Calorimetry. *Nat. Mater.* **2012**, *11*, 279–283.
- (93) Wei, S.; Lucas, P.; Angell, C. A. Phase Change Alloy Viscosities down to  $T_g$  using Adam-Gibbs-Equation Fittings to Excess Entropy Data: A Fragile-to-Strong Transition. *J. Appl. Phys.* **2015**, *118*, No. 034903.
- (94) Orava, J.; Hewak, D. W.; Greer, A. L. Fragile-to-Strong Crossover in Supercooled Liquid Ag-In-Sb-Te Studied by Ultrafast Calorimetry. *Adv. Funct. Mater.* **2015**, *25*, 4851–4858.
- (95) Wei, S.; Evenson, Z.; Stolpe, M.; Lucas, P.; Angell, C. A. Breakdown of the Stokes-Einstein Relation above the Melting Temperature in a Liquid Phase-Change Material. *Sci. Adv.* **2018**, *4*, No. eaat8632.
- (96) Wei, S.; Persch, C.; Stolpe, M.; Evenson, Z.; Coleman, G.; Lucas, P.; Wuttig, M. Violation of the Stokes-Einstein Relation in  $\text{Ge}_2\text{Sb}_2\text{Te}_5$ , GeTe,  $\text{Ag}_4\text{In}_3\text{Sb}_{67}\text{Te}_{26}$  and  $\text{Ge}_{15}\text{Sb}_{85}$ , and its Connection to Fast Crystallization. *Acta Mater.* **2020**, *195*, 491–500.
- (97) Sosso, G. C.; Behler, J.; Bernasconi, M. Breakdown of Stokes-Einstein Relation in the Supercooled Liquid State of Phase Change Materials. *Phys. Status Solidi B* **2012**, *249*, 1880–1885.
- (98) M lek, J.; Shanelova, J. Viscosity of Germanium Sulfide Melts. *J. Non-Cryst. Solids* **1999**, *243*, 116–122.
- (99) Tverjanovich, A. S. Temperature Dependence of the Viscosity of Chalcogenide Glass-Forming Melts. *Glass Phys. Chem.* **2003**, *29*, 532–536.
- (100) Mauro, J. C.; Yue, Y.; Ellison, A. J.; Gupta, P. K.; Allan, D. C. Viscosity of Glass-Forming Liquids. *Proc. Natl. Acad. Sci. U.S.A.* **2009**, *106*, 19780–19784.
- (101) Armstrong, J. K.; Wenby, R. B.; Meiselman, H. J.; Fisher, T. C. The Hydrodynamic Radii of Macromolecules and Their Effect on Red Blood Cell Aggregation. *Biophys. J.* **2004**, *87*, 4259–4270.
- (102) Wei, S.; Lucas, P.; Angell, C. A. Phase-Change Materials: The View from the Liquid Phase and the Metallicity Parameter. *MRS Bull.* **2019**, *44*, 691–698.
- (103) Abrikosov, N. Kh.; Danilova-Dobryakova, G. T.  $\text{Sb}_2\text{Te}_3$ -GeTe Phase Diagram. *Izv. Akad. Nauk SSSR: Neorg. Mater.* **1965**, *1*, 204–209.
- (104) Shelimova, L. E.; Karpinskii, O. G.; Konstantinov, P. P.; Kretova, M. A.; Avilov, E. S.; Zemskov, V. S. Composition and Properties of Layered Compounds in the GeTe- $\text{Sb}_2\text{Te}_3$  System. *Inorg. Mater.* **2001**, *37*, 342–348.
- (105) Boniardi, M. Thermal Model and Remarkable Temperature Effects on the Chalcogenide Alloy. In *Phase Change Memory: Device Physics, Reliability and Applications*; Redaelli, A., Ed.; Springer: Cham, Switzerland, 2018; pp 41–64.
- (106) Alekseev, A.; Fontanari, D.; Sokolov, A.; Bokova, M.; Kassem, M.; Bychkov, E. Ionic Conductivity and Tracer Diffusion in Glassy Chalcogenides. In *World Scientific Reference of Amorphous Materials*; Taylor, P. C., Ed.; World Scientific: Singapore, 2020; Vol. 1, pp 203–249.
- (107) Kassem, M.; Bounazef, T.; Fontanari, D.; Sokolov, A.; Bokova, M.; Hannon, A. C.; Bychkov, E. Chemical and Structural Variety in Sodium Thioarsenate Glasses Studied by Neutron Diffraction and Supported by First-Principles Simulations. *Inorg. Chem.* **2020**, *59*, 16410–16420.
- (108) Stelhorn, J. R.; Paulus, B.; Hosokawa, S.; Pilgrim, W.-C.; Boudet, N.; Blanc, N.; Ikemoto, H.; Kohara, S.; Sutou, Y. Structure of Amorphous  $\text{Cu}_2\text{GeTe}_3$  and the Implications for its Phase-Change Properties. *Phys. Rev. B* **2020**, *101*, No. 214110.
- (109) Koura, A.; Shimojo, F. Intermediate Range Structure of Amorphous  $\text{Cu}_2\text{GeTe}_3$ : Ab Initio Molecular Dynamics Study. *J. Phys.: Condens. Matter* **2020**, *32*, No. 244001.
- (110) Eom, T.; Choi, S.; Choi, B. J.; Lee, M. H.; Gwon, T.; Rha, S. H.; Lee, W.; Kim, M.-S.; Xiao, M.; Buchanan, I.; Cho, D.-Y.; Hwang, C. S. Conformal Formation of  $(\text{GeTe}_2)_{1-x}(\text{Sb}_2\text{Te}_3)_x$  Layers by Atomic Layer Deposition for Nanoscale Phase Change Memories. *Chem. Mater.* **2012**, *24*, 2099–2110.
- (111) Eom, T.; Gwon, T.; Yoo, S.; Choi, B. J.; Kim, M.-S.; Buchanan, I.; Xiao, M.; Hwang, C. S. Influence of the Kinetic Adsorption Process on the Atomic Layer Deposition Process of  $(\text{GeTe}_2)_{1-x}(\text{Sb}_2\text{Te}_3)_x$  Layers Using  $\text{Ge}^{4+}$ -Alkoxide Precursors. *Chem. Mater.* **2014**, *26*, 1583–1591.
- (112) Yoo, S.; Yoo, C.; Park, E.-S.; Kim, W.; Lee, Y. K.; Hwang, C. S. Chemical Interactions in the Atomic Layer Deposition of Ge-Sb-Te Films and Their Ovonic Threshold Switching Behavior. *J. Mater. Chem. C* **2018**, *6*, 5025–5032.